Computers and Geotechnics 181 (2025) 107126

Contents lists available at ScienceDirect

Computers and Geotechnics

journal homepage: www.elsevier.com/locate/compgeo

Research Paper

Microscopic analysis of granular material behaviour from small to large strains

Qing Chen [a], Chao Zhou [b,*]

[a] Department of Civil and Environmental Engineering The Hong Kong Polytechnic University Hung Hom Kowloon Hong Kong

[b] Department of Civil and Environmental Engineering Research Institute for Sustainable Urban Development The Hong Kong Polytechnic University Hung Hom Hong Kong

ARTICLE INFO

Keywords:
Small-strain stiffness
Large-strain behaviour
Discrete element method

ABSTRACT

The Discrete Element Method (DEM) has been widely used to study the macro–micro behaviour of granular materials at large strains (>1%). However, investigations over a wider strain range are lacking. This study conducts DEM triaxial tests on specimens with different particle physical properties to examine their influence on macro–micro behaviour from small strains (below 1 %) to large strains. Small-strain behaviour is characterised by the maximum shear modulus, elastic range and stiffness degradation rate. Large-strain behaviour is analysed through the peak stress ratio, critical state stress ratio and void ratio. Then, the micro-mechanisms underlying these results are examined using the Stress-Force-Fabric (SFF) relationship, which links the (macro) stress ratio and (micro) anisotropy source. This study is the first to apply the SFF relationship to small strain behaviour. Results reveal the qualitative relationship between particle physical properties and macro-behaviour at different strains: increasing particle Young's modulus enhances the maximum shear modulus but accelerates stiffness degradation; increasing shearing and rolling friction significantly reduces the stiffness degradation at small strains and enhances strength and dilation at large strains. This study also highlights the limitation of the Hertz contact model in capturing both small-strain and large-strain behaviour quantitatively using a single set of parameters. Hence, modellers should calibrate model parameters based on whether their focus is on large-strain or small-strain behaviour. For micro-behaviour, the relative importance of anisotropy sources depends on strain level rather than particle physical properties. At small strains, the mechanical anisotropy source (both normal and tangential forces) primarily controls stiffness and its degradation. At large strains, material strength is influenced by both mechanical and geometrical anisotropy sources, with anisotropy from the normal force being the most significant, followed by contact normal, tangential forces, and branch vector.

1. Introduction

Granular materials, such as sand, are ubiquitous in natural environments and industrial applications. The mechanical behaviour of granular materials is of both theoretical interest and practical importance in fields such as civil engineering, geophysics, and materials science and geo-energy engineering (Cui et al., 2023; da Cruz et al., 2005; Dai et al., 2024; Radjai et al., 2017; Thornton and Antony, 1998). It has been investigated by many researchers, focusing on different aspects under different strain levels. At large strains, the strength, dilatancy, and critical state have received significant interest (Bolton, 1986; Fu and Dafalias, 2011; Li and Dafalias, 2012; Wood, 1990). At small strains, the degradation characteristics of stiffness become a focus since it is well-known that soil stiffness decreases with increasing strain by two to three orders of magnitude (Atkinson, 2000; Bentil et al., 2023; Bentil and Zhou, 2022; Clayton, 2011; Ng et al., 2020; Oztoprak and Bolton, 2013; Yimsiri and Soga, 2000; Zhou et al., 2015).

The DEM has proven to be a valuable tool for studying and quantifying the complex macro–micro mechanical behaviour of granular material (O'Sullivan, 2011). As a result, DEM has been widely used in studying the large-deformation behaviour of granular materials (Cheng et al., 2004; Thornton and Antony, 1998; Wang et al., 2017; Wang et al., 2016) and also the small-strain behaviour but which is received comparatively less attention (Gu et al., 2013; Nguyen, 2022; Nie et al., 2024; Otsubo et al., 2017; Reddy et al., 2022; Sitharam and Vinod, 2010; Zhou and Xu, 2024).

In the DEM simulations, the computed macro-behaviour is fundamentally determined by the interactions between particles and their physical properties (i.e., contact model parameters) (Wu et al., 2022). So

* Corresponding author.
E-mail addresses: qqing.chen@connect.polyu.hk (Q. Chen), c.zhou@polyu.edu.hk (C. Zhou).

https://doi.org/10.1016/j.compgeo.2025.107126
Received 27 September 2024; Received in revised form 23 December 2024; Accepted 28 January 2025
Available online 16 February 2025

Nomenclature

$\boldsymbol{A}^{[*]}$	Anisotropy tensors
$a_{[*]}$	Second invariant of the anisotropy tensors
d	Mean particle diameter
E_p	Youngs' modulus of particle
e_c	Critical state void ratio
F_n, F_s	Normal force and shear force at contact
$\bar{f}_i(\boldsymbol{n})$	Distribution functions of contact force
$\bar{b}_i(\boldsymbol{n})$	Distribution functions of branch vectors
$E(\boldsymbol{n})$	Distribution functions of contact normal
$G_{\sec}$	Secant shear modulus
G_0	Maximum secant shear modulus
I	Inertia number
k_n, k_s, k_r	Resultant normal, tangential and rolling stiffness
M_r	Rolling moment at contact
M_p	Peak stress ratio
M_c	Critical state stress ratio
m	Curvature parameter of the stiffness degradation curve
N_c	Number of the contact
$\boldsymbol{n}$	Contact normal vector
p'	Mean effective stress
q	Deviatoric stress
V	Volume of the specimen
X_{norm}	Normalized micro-contact parameters
Y_{norm}	Normalized macro features
α_r	Dimensionless rolling stiffness coefficient parameter
β_0, β_i	Fitting parameter of the linear multiple regression
$\dot{\gamma}$	Loading rate
γ_e	Elastic shearstrain of the stiffness degradation curve
γ_r	Reference shear strain of the stiffness degradation curve
δ_n	Relative normal displacement
$\Delta\delta_s$	Relative incremental relative tangential displacement
$\Delta\theta_r$	Relative incremental relative rotation
$\boldsymbol{\delta}$	Kronecker Delta
$\varepsilon_a, \varepsilon_v, \varepsilon_q$	Deviatoric strain, volumetric strain and axial strain
η	Stress ratio
μ_r	Rolling friction coefficient
μ_s	Shear friction coefficient
ν	The Poisson's ratio of particle
$\boldsymbol{\sigma}$	Stress tensor
σ^0	Magnitude of the isotropic state stress component
$\boldsymbol{\sigma}^0$	Isotropic state stress component
$\boldsymbol{\sigma}^c$	Stress component of contact normal
$\boldsymbol{\sigma}^b$	Stress component of branch vector
$\boldsymbol{\sigma}^f$	Stress component of contact force

far, some research has examined the influences of contact model parameters on granular material behaviour at either small strain (Gong et al., 2024; Otsubo and O'Sullivan, 2018; Reddy et al., 2022) or large strain (Antony and Kruyt, 2009; Hartmann et al., 2022; Mohamed and Gutierrez, 2010; Plassiard et al., 2009; Wensrich and Katterfeld, 2012). These previous parametric studies focus on one strain level, and the parameters in DEM simulations are often calibrated to match the observed experimental results. However, the calibration results for small and large strains may differ significantly. For instance, the calibrated value of particle Young's modulus can be up to 140 GPa at small strains (Reddy et al., 2022) but can be as low as 4 GPa at large strains (Gu et al., 2020; Hartmann et al., 2022; Cheng et al., 2017). With the aim of understanding granular material behaviour and improving the modelling capability, it is necessary to explore whether common contact model like the Hertz model can accurately model both small-strain and large-strain behaviour using a single set of model parameters. If not, it is important to understand the extent to which we can model the behaviour and which features of the behaviour cannot be accurately represented. To address these questions, it is crucial to fully understand the influences of particle physical properties on the mechanical behaviour of granular materials across different strain levels. This forms the motivation of this paper to conduct a comprehensive parametric study on specimens from small to large strains.

In addition to the influence of particle physical properties on macro-behaviour, some studies have also aimed at understanding the micro-mechanisms in granular materials. Based on the results at large strains, it has been well recognised that anisotropy at a microscopic level has a significant influence on the macro-behaviour of granular material, such as critical state (Li and Dafalias, 2012; Li and Dafalias, 2015), liquefaction and phase transformation behaviour (Guo and Zhao, 2013; Sitharam et al., 2009). The anisotropy in the granular can be classified into geometrical anisotropy (fabric expressed by the direction of contact normal and branch vectors) and mechanical anisotropy (induced by external force and related to contact force). The SFF framework, which builds an analytical correlation between the anisotropy and shear strength, has been widely used to study the macro–micro behaviour at large strains (Guo and Zhao, 2013; Li and Yu, 2011; Ouadfel and Rothenburg, 2001; Sitharam et al., 2009). For instance, based on SFF, numerous studies have demonstrated that mechanical anisotropy is a dominant contributor to shear resistance in granular materials (Guo and Zhao, 2013; Ouadfel and Rothenburg, 2001; Sufian et al., 2017; Zhao et al., 2018), whereas geometric anisotropy related to branch vector has a negative impact on shear strength (Ouadfel and Rothenburg, 2001; Zhao et al., 2018). However, the application of the SFF framework at small strains is lacking. So far, some researchers have explored the change of a specific anisotropy, such as contact normal anisotropy, at small strains (Li et al., 2022; Nguyen, 2022; Reddy et al., 2022; Zhou and Xu, 2024). This micro information is useful for understanding the small strain stiffness behaviour, but they are not comprehensive enough to explain the stiffness and its degradation. The SFF framework may provide an analytical tool to address this problem. Thus, a unified SFF analysis in both small and large strains is required to provide new insights into the contribution of anisotropy source of granular materials across different strain levels. In addition, the influence of contact model parameters on each form of anisotropy source needs to be understood.

Given the above discussion, this study aims to address several scientific questions: (1) how do particle physical properties affect the mechanical behaviour of granular materials across different strain levels? (2) is it possible to accurately model both small-strain and large-strain behaviour using a single set of model parameters? (3) is the SFF framework valid at small strains? (4) how do anisotropic sources affect the stiffness characteristics at small strains? (5) how do contact model parameters affect each anisotropy source from small to large strains?

This paper begins with a detailed description of the DEM simulation of triaxial tests conducted using the open-source DEM package YADE (Šmilauer et al., 2015). A series of triaxial tests were performed to investigate the behaviour of granular materials under varying stress levels and physical properties at both small and large strain conditions. Following this, an overview of the SFF relationship is provided, along with its validation. The typical relationship between micro anisotropy and macro stiffness, as well as between micro anisotropy and macro strength, is also presented. Subsequently, the influence of particle properties on the macro–micro behaviour of granular materials is examined, focusing on small strain stiffness behaviour and the stress–-strain relationship at large strains. The paper concludes with a summary of the most salient findings.

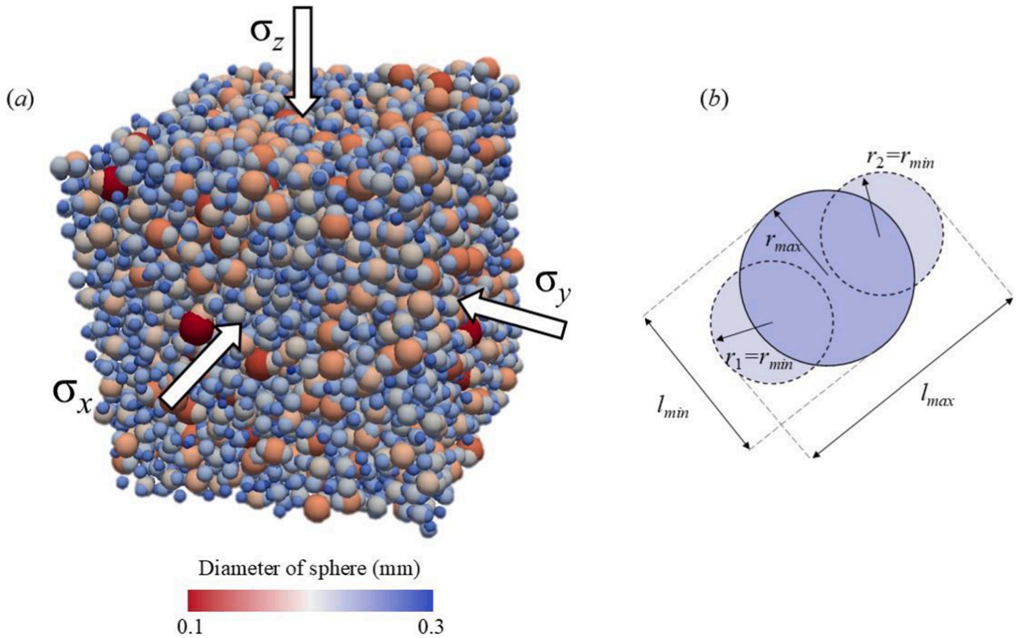

Fig. 1. (a) Schematic of a DEM specimen before shearing and (b) 2D schematic diagram of the particle shape defined in this study.

Table 1
Summary of the contact model parameter analysis in DEM simulations.

Parameter	E_p (GPa)	μ_s	α_r	μ_r
Reference case	70	0.3	1.0	0.5
Young's modulus, E_p	0.7, 7.0, 70	0.3	1.0	0.5
Shearing friction, μ_s	70	0.1, 0.3, 0.5, 0.7	1.0	0.5
Rolling stiffness, α_r	70	0.3	0.1, 0.5, 1.0	0.5
Rolling friction, μ_r	70	0.3	1.0	0.1, 0.5, 0.9

Table 2
Approximation of the distribution function and the corresponding anisotropy tensor.

Approximation for the distribution function		Calculation of anisotropy tensor	
Contact normal			
$E(\boldsymbol{n}) = \frac{1}{4\pi}\left(1 + A^{c}_{ij} n_i n_j\right)$	(T1)	$A^{c}_{ij} = \frac{15}{2}\left[\phi^{c}_{ij} - \frac{\phi^{c}_{kk}}{3}\delta_{ij}\right]$	(T2)
		$\phi^{c}_{ij} = \frac{1}{N_c}\sum_{\alpha=1}^{N_c} n^{\alpha}_i n^{\alpha}_j$	(T3)
Contact forces			
$\bar{f}^{n}(\boldsymbol{n}) = \bar{f}^{n}_0\left[1 + A^{f_n}_{ij} n_i n_j\right]$	(T4)	$A^{f_n}_{ij} = \frac{15}{2\bar{f}^{n}_0}\left[K^{n}_{ij} - \frac{K^{n}_{kk}}{3}\delta_{ij}\right]$	(T5)
		$K^{n}_{ij} = \frac{1}{N_c}\sum_{\alpha=1}^{N_c}\frac{f^{n,\alpha} n^{\alpha}_i n^{\alpha}_j}{1 + A^{c}_{kl} n^{\alpha}_k n^{\alpha}_l}$	(T6)
		$\bar{f}^{n}_0 = K^{n}_{ii}$	(T7)
$\bar{f}^{t}_i(\boldsymbol{n}) = \bar{f}^{n}_0\left[A^{f_t}_{ik} n_k - \left(A^{f_t}_{kl} n_k n_l\right) n_i\right]$	(T8)	$A^{f_t}_{ij} = \frac{15}{3\bar{f}^{0}_n}\left[K^{t}_{ij} - \frac{K^{t}_{kk}}{3}\delta_{ij}\right]$	(T9)
		$K^{t}_{ij} = \frac{1}{N_c}\sum_{\alpha=1}^{N_c}\frac{f^{t,\alpha} t^{\alpha}_i n^{\alpha}_j}{1 + A^{c}_{kl} n^{\alpha}_k n^{\alpha}_l}$	(T10)
Branch vectors			
$\bar{b}^{n}(\boldsymbol{n}) = \bar{b}^{n}_0\left(1 + A^{b_n}_{ij} n_i n_j\right)$	(T11)	$A^{b_n}_{ij} = \frac{15}{2\bar{b}^{n}_0}\left[D^{n}_{ij} - \frac{D^{n}_{kk}}{3}\delta_{ij}\right]$	(T12)
		$D^{n}_{ij} = \frac{1}{N_c}\sum_{\alpha=1}^{N_c}\frac{b^{n,\alpha} n^{\alpha}_i n^{\alpha}_j}{1 + A^{c}_{kl} n^{\alpha}_k n^{\alpha}_l}$	(T13)
$\bar{b}^{t}_i(\boldsymbol{n}) = \bar{b}^{n}_0\left[A^{b_t}_{ik} n_k - \left(A^{b_t}_{kl} n_k n_l\right) n_i\right]$	(T14)	$A^{b_t}_{ij} = \frac{15}{3\bar{b}^{n}_0}\left[D^{t}_{ij} - \frac{D^{t}_{kk}}{3}\delta_{ij}\right]$	(T15)
		$D^{t}_{ij} = \frac{1}{N_c}\sum_{\alpha=1}^{N_c}\frac{b^{t,\alpha} t^{\alpha}_i n^{\alpha}_j}{1 + A^{c}_{kl} n^{\alpha}_k n^{\alpha}_l}$	(T16)
		$\bar{b}^{n}_0 = D^{n}_{ii}$	(T17)

2. Details of numerical simulation

2.1. Simulation procedures of triaxial test

The drained triaxial test using DEM in this study comprises four stages: (1) particle generation, (2) specimen packing, (3) isotropic compression, and (4) triaxial shearing test. Firstly, a predetermined number (3,656) of non-spherical particles that represent sand grains were randomly generated without overlap within a cubic box featuring periodic boundaries. The implementation of periodic boundaries helps to reduce the required particle number by mitigating boundary effects and prevents strain localisation during the shearing process (Modenese, 2013; Thornton and Zhang, 2006).

Non-spherical particles were selected to reflect the natural structure of the sand. The focus of this study is the influence of particle physical properties, so a simple clump-based shape was employed to approximate the aspect ratio and roundness of Toyoura sand, similar to previous works (Azéma and Radjaï, 2010; Kodicherla et al., 2019). The chosen particle shape is a compromise between the realistic morphology modelling of actual particles and the high computational time of DEM simulations. As depicted in Fig. 1, a clump particle consists of three aligned spherical members, with the spheres at both ends being of equal diameter. The aspect ratio ($AR = l_{min}/l_{max}$) and roundness ($Ro = \frac{\sum r_i/N}{r_{max}} = \frac{r_{min}}{r_{max}}$) were set to 0.74 and 0.70, respectively, in alignment with the average value observed in Toyoura sand (Altuhafi Fatin et al., 2016; Le et al., 2020). It should be noted that the particle size is characterised by the minimum axis length of the clump, i.e., the size of the largest sphere within the clump. With reference to natural Toyoura sand, the particle size distributes within the range from 0.1 to 0.3 mm. During generation, the major orientation of particles adjusted to the horizontal, and specific orientations within the horizontal plane were randomly assigned to mimic the natural fabric of sand under gravity. Particle density (2,650 $\times$ 10^3 kg/m^3) is scaled up by a factor of 1,000, which is a widely adopted technique to increase timestep and accelerate the quasi-

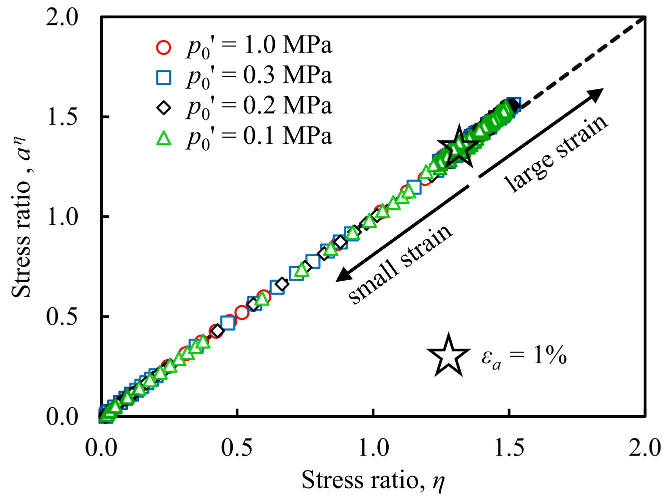

Fig. 2. The relationship between stress ratio (η) and calculated stress ratio (a^η) based on the SFF relationship for reference cases under different pressure.

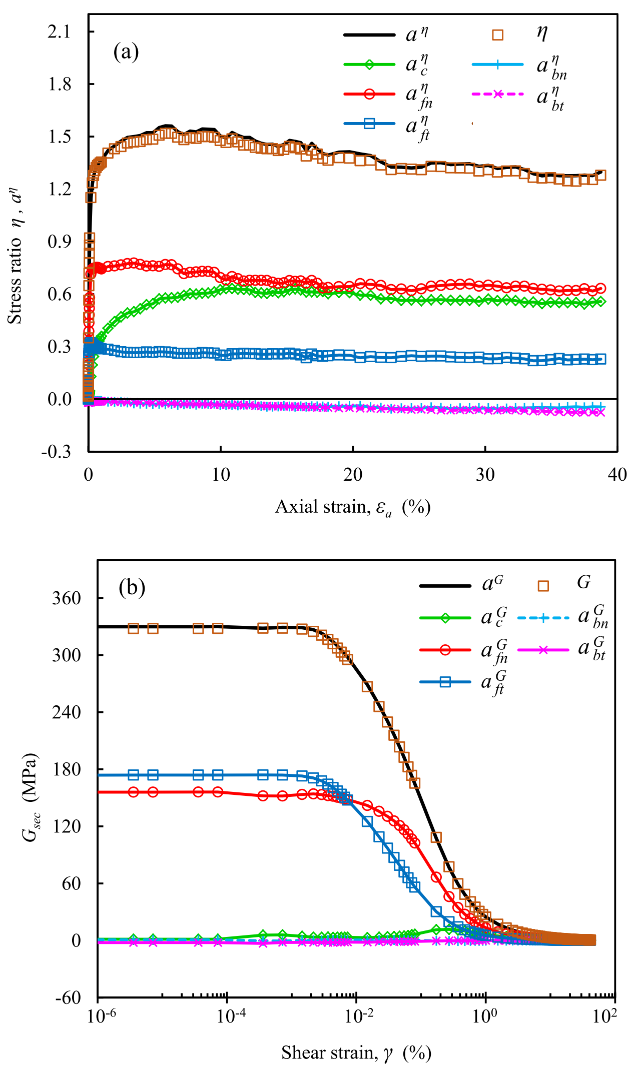

Fig. 3. Typical SFF for reference case under $p_0' = 300$ kPa: (a) stress ratio at large strains and (b) shear modulus at small strains.

Table 3
Summary of variables describing the macro–micro behavior at small and large strains.

	Small strains	*Large strains*
Macro behavior	G_0, γ_e, γ_r, m	M_p, ε_{peak}, M_c, e_c, $e_c^{rattler}$
Micro behavior	a_c^G, a_{fn}^G, a_{ft}^G	a_c^η, a_{fn}^η, a_{ft}^η

static process (O'Sullivan, 2011; Thornton and Antony, 2000).

At the stage of specimen packing, the specimen is subjected to isotropic compression to a predetermined confining pressure of 10 kPa, a value often employed by other researchers (Gu et al., 2020). In this step, the friction parameters, including both shearing and rolling friction, are adjusted to different values to create specimens with varying relative densities (Modenese, 2013). The maximum and minimum void ratios are attained by adopting the maximum friction parameter (equivalent to the original values of friction parameters used in the subsequent process) and minimum friction parameter (set to zero), respectively. Upon completion of the packing, the friction parameters are reset to their original values and maintain constant throughout the subsequent loading process.

After that, the specimen undergoes isotropic compression to reach a target pressure. Finally, the specimen is subjected to triaxial compression/shear. During the loading process, the quasi-static condition is maintained by applying a low loading rate. The load rate is determined according to Inertia number $I = \dot{\gamma} d\sqrt{\rho/p'}$, where $\dot{\gamma}$ is the loading rate, d is the mean particle diameter, ρ is the particle density, and p' is the mean effective stress (da Cruz et al., 2005). The threshold of I is typically 10^{-3} to ensure the quasi-static condition (Yang et al., 2021), and the value chosen in this study is 10^{-4}.

2.2. Contact models

During the above simulation procedure, the interaction between particles is modelled using the Hertz-Mindlin contact model with Mohr-Coulomb sliding friction and rolling resistance (Johnson, 1987; Modenese, 2013). The contact model computes the normal force F_n, shear force F_s (Cundall, 1988; Mindlin and Deresiewicz, 1953) and rolling moment M_r (Belheine et al., 2009; Iwashita and Oda, 1998) at the contacts as follows:

$$F_n = \begin{cases} 2/3k_n\delta_n, \delta_n < 0 \\ 0, \delta_n \geq 0 \end{cases} \quad (1)$$

$$\Delta F_s = \begin{cases} k_s\Delta\delta_s, F_s < |F_n|\mu_s \\ 0, F_s \geq |F_n|\mu_s \end{cases} \quad (2)$$

$$\Delta M_r = \begin{cases} k_r\Delta\theta_r, M_r < |F_n|R_e\mu_r \\ 0, M_r \geq |F_n|R_e\mu_r \end{cases} \quad (3)$$

The contact motion terms δ_n, $\Delta\delta_s$, and $\Delta\theta_r$ represent the relative normal displacement, the incremental relative tangential displacement and the incremental relative rotation, respectively. Correspondingly, the variables k_n, k_s, and k_r denote the resultant normal stiffness, tangential stiffness and rolling stiffness, respectively. The maximum shear force and the maximum rolling moment are both related to the normal contact force and can be characterised by a failure criterion that follows the Mohr-Coulomb form (Estrada et al., 2008; Iwashita and Oda, 1998), as shown in Eq. (2) and Eq. (3), respectively. Here, μ_s represents the interparticle friction coefficient; while μ_r is the rolling friction coefficient, which dictates the threshold for the plastic tangential force and rolling moment, respectively.

The calculation of the resultant stiffness term (k_n, k_s and k_r) is presented in Eqs. (4–6):

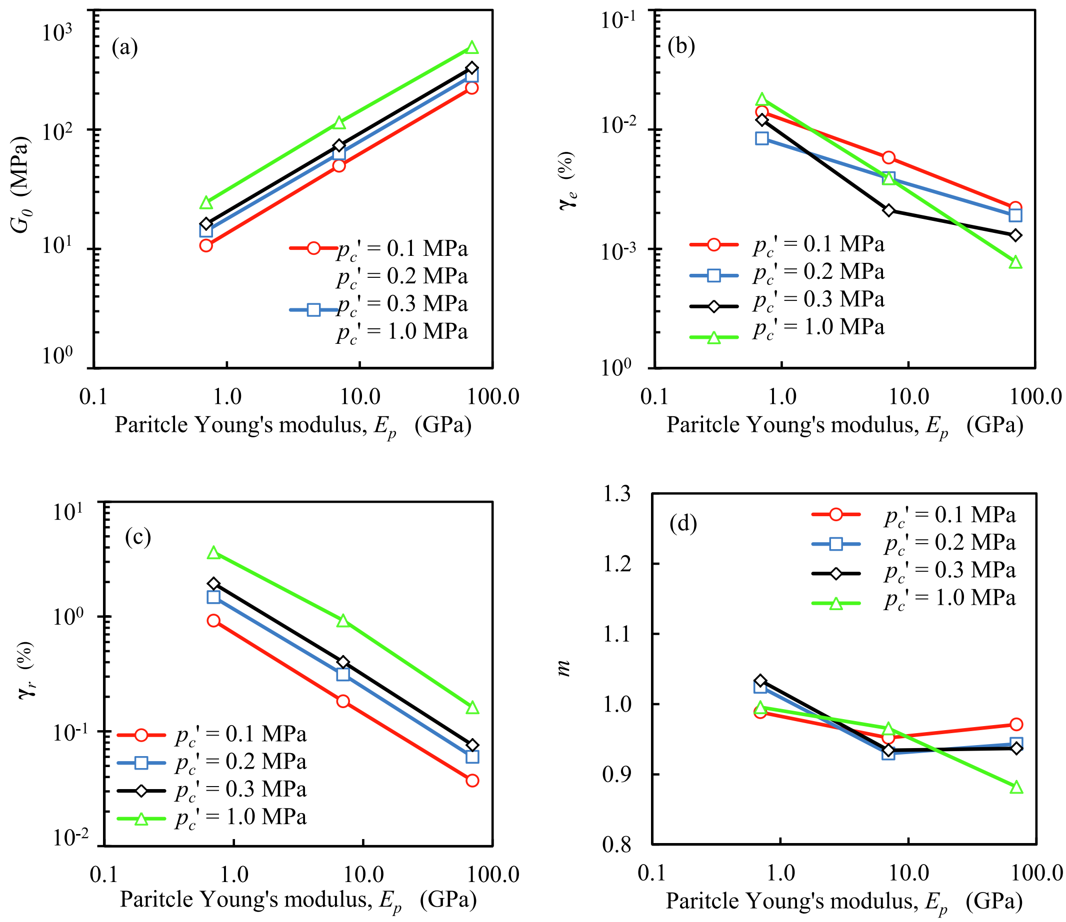

Fig. 4. The influence of particle Young's modulus E_p on the small strain stiffness behaviour: (a) G_0 , (b) γ_e , (c) γ_r , (d) m.

$$k_n = 2E_c\sqrt{R_e}\delta_n^{\frac{1}{2}} \tag{4}$$

$$k_s = 8G_e\sqrt{R_e}\delta_n^{\frac{1}{2}} \tag{5}$$

$$k_r = \alpha_r k_s R_e^2 \tag{6}$$

where parameter α_r is a dimensionless coefficient parameter for the rolling stiffness. The expressions for the three stiffness coefficients incorporate the equivalent particle radius R_e, the equivalent effective Young's modulus E_e and the equivalent effective shear modulus G_e, which are defined as follows:

$$R_e = \left(\frac{1}{R_1} + \frac{1}{R_2}\right)^{-1} \tag{7}$$

$$E_e = \left(\frac{1-\nu_1^2}{E_1} + \frac{1-\nu_2^2}{E_2}\right)^{-1} \tag{8}$$

$$G_e = \left(\frac{2(1+\nu_1)(2-\nu_1)}{E_1} + \frac{2(1+\nu_1)(2-\nu_1)}{E_2}\right)^{-1} \tag{9}$$

where E_1 and E_2 are the Young's moduli of the contacted particles 1 and 2, respectively; R_1 and R_2 denote the radius of these particles; ν_1 and ν_2 are their Poisson's ratios. It should be noted that each clump member (sphere) employs the contact model introduced above to determine the interaction forces and moments. The forces and moments influence the whole clump. The spheres within the same clump do not interact with each other.

2.3. Numerical programs of triaxial test

According to Section 2.2, there are five parameters (E_p, ν, μ_s, μ_r, α_r) in the contact model totally. A parametric study with a total of 52 simulations was conducted to examine the influence of these contact model parameters on the macro–micro behaviour at different strain levels, as summarised in Table 1. When examining the influences of a specific parameter, all other variables are constant and equal to the values in the reference case. The choice of these values is considering the typical range observed in quartz sand (Reddy et al., 2022; Sandeep et al., 2018; Sandeep and Senetakis, 2018a; Sandeep and Senetakis, 2018b) and the typical values utilised in DEM simulations (Hartmann et al., 2022; Huang et al., 2014; Cheng et al., 2017; Rorato et al., 2021; Thornton, 2000). A preliminary study shows that Poisson's ratio (ν) has a minimal influence on the results; therefore, this parameter has been excluded from our analysis. Additionally, to explores the impact of initial confining pressure (p_0'), four values were selected: 0.1, 0.2, 0.3, and 1 MPa. In the subsequent section, only the results from the dense specimens are presented, as there is a particular interest in the strain-softening behaviour observed at large strains. The dense state of the specimen was generated by setting the friction μ_s to varying small value (<0.05) and μ_r equivalent to 0 before isotropic compression. This step can also ensure that the void ratio of all the specimens remains consistent (around 0.57 to 0.59).

3. Macro-micro analysis approach: SFF relationship

To investigate the contribution of different forms of micro anisotropy to the macroscopic stiffness and strength across small to large strain ranges, this study employs the SFF relationship. The following section

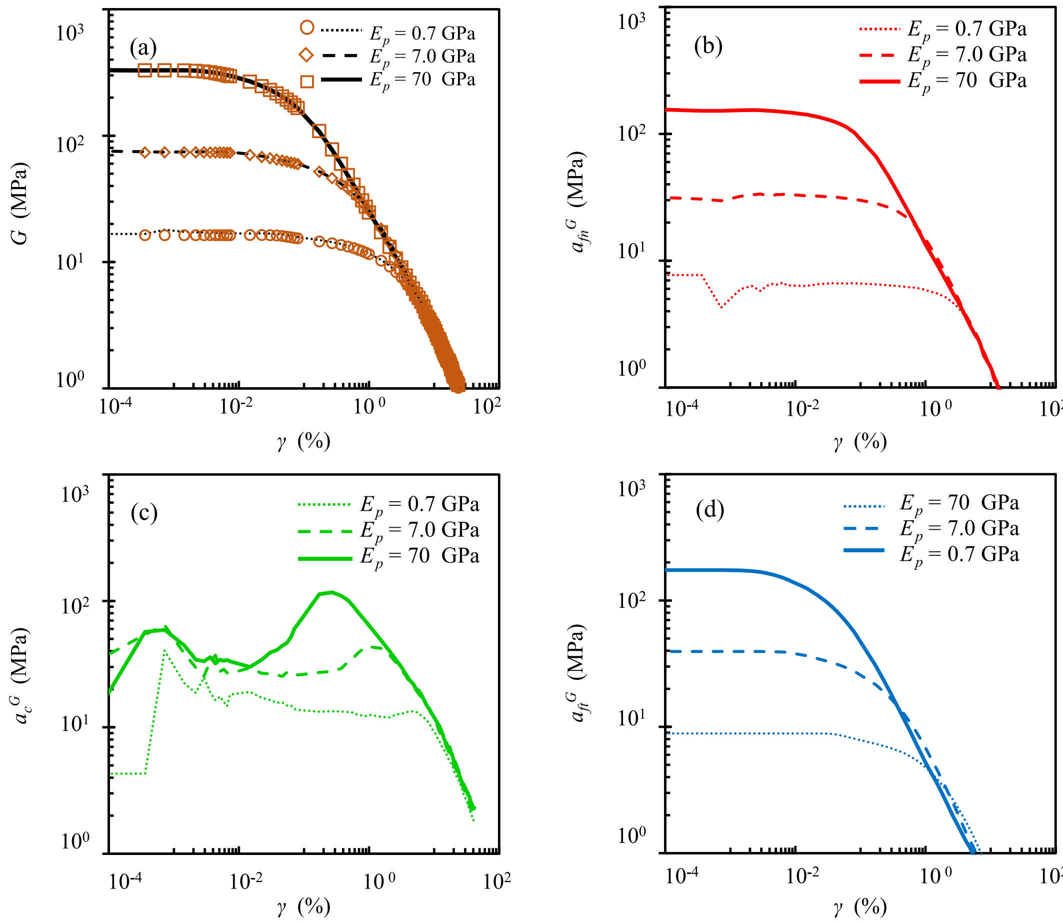

Fig. 5. The influence of particle Young's modulus E_p on the contribution from each anisotropy source to the small strain stiffness at $p_0{}' = 0.3$ MPa: (a) overall DEM result (marker) and SFF result (line); (b) a_{fn}^G, (c) a_c^G, (d) a_{ft}^G.

provides a brief overview of the SFF relationship, while a comprehensive derivation and explanation can refer to the works of Ouadfel and Rothenburg (2001) or Li and Yu (2011). Then, a validation of the SFF relationship and typical results will also be presented. For the first time, the SFF relationship is extended to investigate the small strain stiffness behaviour.

3.1. Decomposition of stress tensor

The SFF relationship expresses the stress tensor of granular materials as follows:

$$\sigma_{ij} = \frac{N_c}{V}\int_n \overline{f}_i(\boldsymbol{n})\overline{b}_j(\boldsymbol{n})E(\boldsymbol{n})\mathrm{d}\boldsymbol{n} \tag{10}$$

where N_c represent the number of contacts; V denotes the volume of specimen; and $\overline{f}_i(\boldsymbol{n})$, $\overline{b}_j(\boldsymbol{n})$ and $E(\boldsymbol{n})$ correspond to the distribution functions of contact force, branch vectors and contact normal, respectively; $\boldsymbol{n}$ is the contact normal vector (while d$\boldsymbol{n}$ can be treated as a solid angle element). Eq. (10) indicates that the overall stress is a product of the combined effects of various microscopic anisotropy sources. By introducing an appropriate analytical approximation for the distribution functions in Eq. (10) and subsequently integrating it, an explicit relationship between macroscopic stress and microscopic anisotropy can be derived. Following Ouadfel and Rothenburg (2001), the distribution function can be devided into: an isotropic term ($1/4\pi, \overline{f}_0^{\mathrm{n}}n_i$ and $\overline{b}_0^{\mathrm{n}}n_j$) and a deviatoric term ($E^*(\boldsymbol{n}), \overline{f}_i^*(\boldsymbol{n})$ and $\overline{b}_j^*(\boldsymbol{n})$):

$$E(\boldsymbol{n}) = \frac{1}{4\pi} + E^*(\boldsymbol{n}) \tag{11a}$$

$$\overline{f}_i(\boldsymbol{n}) = \overline{f}_0^{\mathrm{n}}n_i + \overline{f}_i^*(\boldsymbol{n}) \tag{11b}$$

$$\overline{b}_j(\boldsymbol{n}) = \overline{b}_0^{\mathrm{n}}n_j + \overline{b}_j^*(\boldsymbol{n}) \tag{11c}$$

Then, substituting the distribution functions in Eq. (11a-c) into Eq. (10), the stress tensor becomes

$$\sigma_{ij} = \frac{N_c}{V}\int_n \left[\overline{f}_0^{\mathrm{n}}n_i + \overline{f}_i^*(\boldsymbol{n})\right]\left[\overline{b}_0^{\mathrm{n}}n_j + \overline{b}_j^*(\boldsymbol{n})\right]\left[\frac{1}{4\pi} + E^*(\boldsymbol{n})\right]\mathrm{d}\boldsymbol{n} \tag{12a}$$

Next, by performing the product and then integrating Eq. (12a), the stress tensor can be decomposed into $2^3 = 8$ terms, denoted as follows:

$$\sigma_{ij} = \sigma_{ij}^0 + \sigma_{ij}^c + \sigma_{ij}^b + \sigma_{ij}^f + \sigma_{ij}^{cb} + \sigma_{ij}^{cf} + \sigma_{ij}^{fb} + \sigma_{ij}^{cfb} \tag{12b}$$

where σ_{ij}^0 is a spherical component which corresponds to an isotropic state; the deviatoric anisotropy tensors σ_{ij}^c, σ_{ij}^b, and σ_{ij}^f, represents the contribution of individual anisotropy from ***c***ontact normal, ***b***ranch vector and contact ***f***orce, respectively. The remaining anisotropy tensors, denoted as σ_{ij}^{cb}, σ_{ij}^{cf}, σ_{ij}^{fb}, σ_{ij}^{cfb} are defined as the pair or trio products of anisotropy-related quantities, for example, the superscript '*cb*' of tensor σ_{ij}^{cb} mean the tensor presenting the overall contribution from both the contact normal and branch vector.

The components (σ_{ij}^{cb}, σ_{ij}^{cf}, σ_{ij}^{fb}, σ_{ij}^{cfb}) of the high-order products of the basic tensor are generally considered negligible small and can be

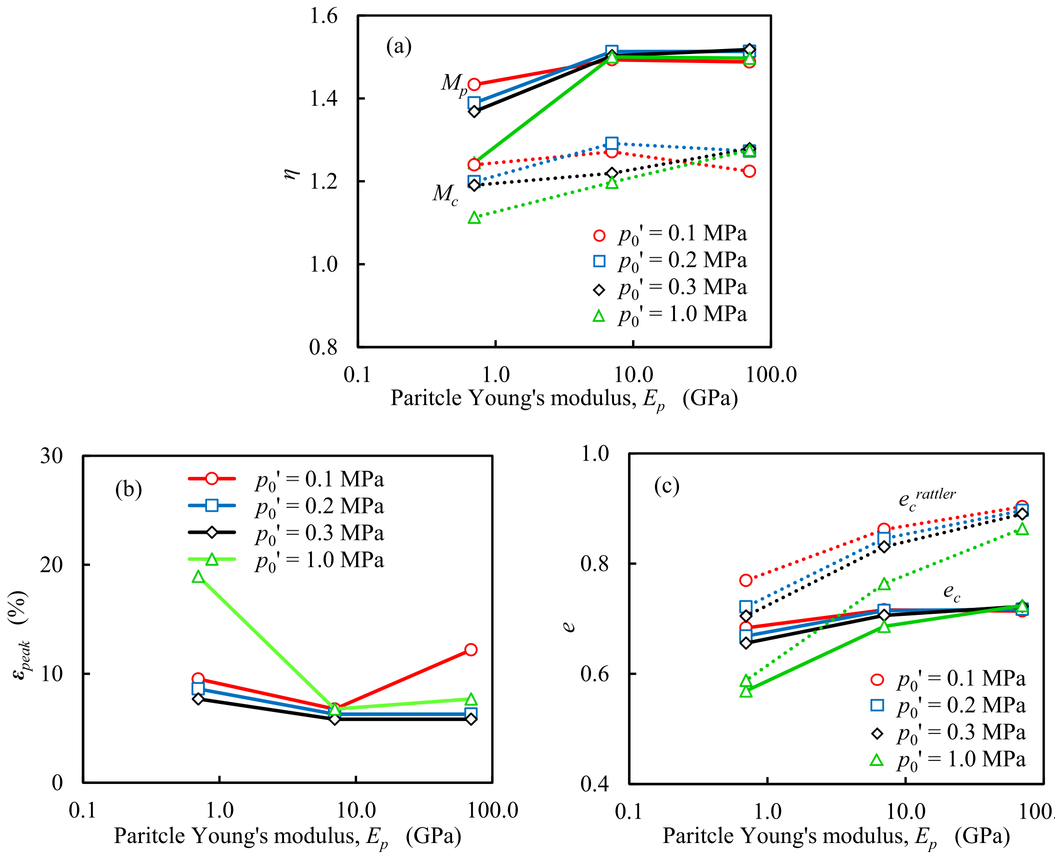

Fig. 6. The influence of particle Young's modulus E_p on the large-strain behaviour: (a) M_p (solid line) and M_c (dash line); (b) $\varepsilon_{\text{peak}}$; (c) e_c (solid line) and e_c^{rattler} (dash line).

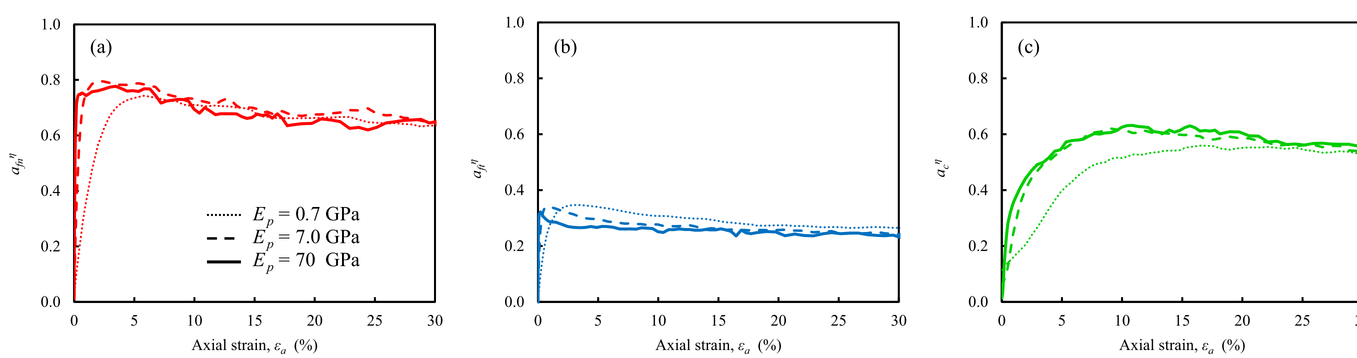

Fig. 7. The influence of particle Young's modulus E_p on the anisotropy source at large strain ($p_0{'} = 0.3$ MPa): (a) $a_{f_n}^{\eta}$; (b) $a_{f_t}^{\eta}$; and (c) a_c^{η}.

ignored (Guo and Zhao, 2013; Sufian et al., 2017). Therefore, these terms are omitted in this study, allowing Eq. (12b) to be simplified as follows:

$$\sigma_{ij} = \sigma_{ij}^0 + \sigma_{ij}^c + \sigma_{ij}^b + \sigma_{ij}^f \tag{13}$$

Currently, the stress tensor has been decomposed into four components, but the calculation of each component is still unknown. As introduced above, an appropriate analytical approximation for the distribution functions in Eqs. (11a-c) is needed. The deviatoric part of the distribution for the contact force, branch vectors and contact normal is usually quantified by their corresponding "anisotropy tensors", as follows:

$$E(\boldsymbol{n}) = \frac{1}{4\pi} + E^{*}(\boldsymbol{n}) = \frac{1}{4\pi}\left(1 + A_{ij}^{c} n_i n_j\right) \tag{14a}$$

$$\bar{f}_i(\boldsymbol{n}) = \bar{f}_0^{n} n_i + \bar{f}_i^{*}(\boldsymbol{n}) = \bar{f}_0^{n} n_i + \bar{f}_0^{n}\left[A_{ik}^{f_t} n_k + \left(A_{kl}^{f_n} - A_{kl}^{f_t}\right) n_k n_l n_i\right] \tag{14b}$$

$$\bar{b}_j(\boldsymbol{n}) = \bar{b}_0^{n} n_j + \bar{b}_j^{*}(\boldsymbol{n}) = \bar{b}_0^{n} n_j + \bar{b}_0^{n}\left[A_{jk}^{b_t} n_k + \left(A_{kl}^{b_n} - A_{kl}^{b_t}\right) n_k n_l n_j\right] \tag{14c}$$

Here, the superscript of each anisotropy tensor, c, b_n, b_t, f_n, f_t, stand for the contact normal, normal branch vectors, tangential branch vectors, normal contact force and tangential contact forces, respectively. Knowing the relationship between the distribution functions and the anisotropy tensor, each stress component in Eq. (13) can expressed in terms of anisotropy tensors as follows (Ouadfel and Rothenburg, 2001):

$$\sigma_{ij}^0 = \sigma^0 \delta_{ij} = \frac{N_c \bar{f}_0^{n} \bar{b}_0^{n}}{V} \delta_{ij} \tag{15}$$

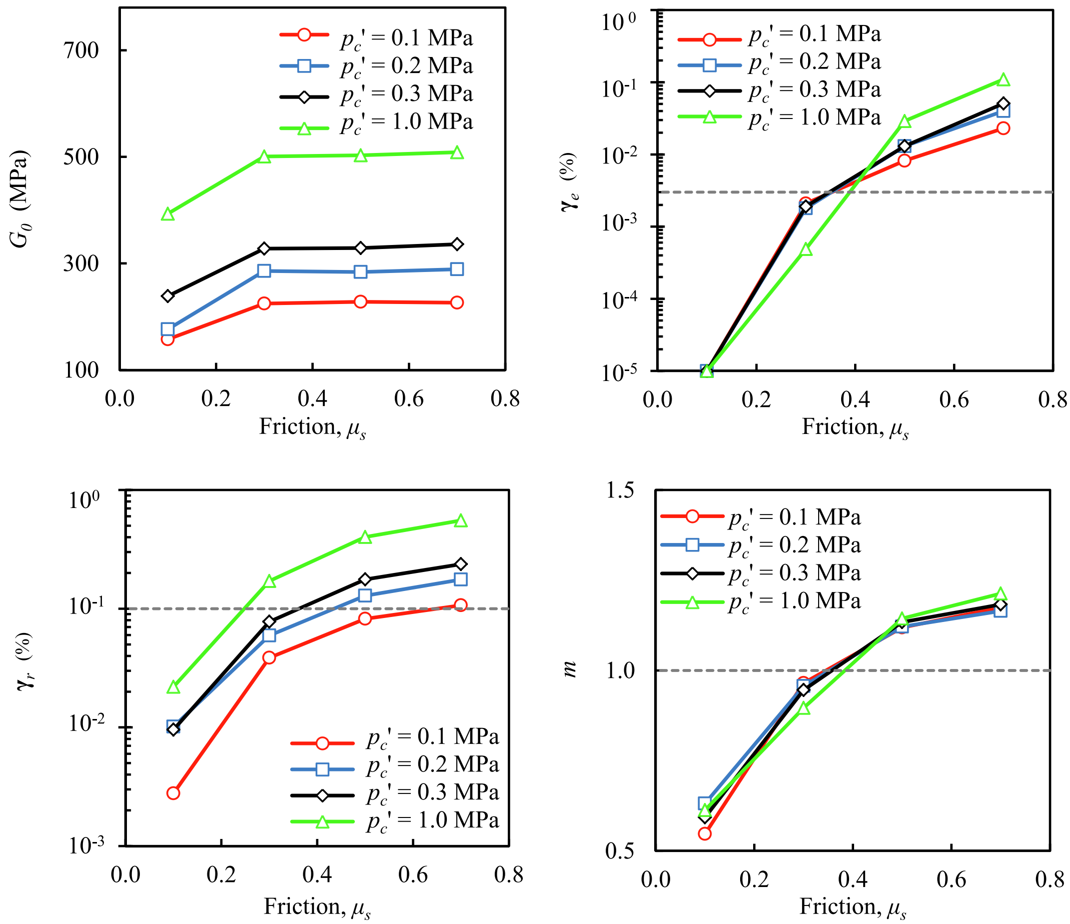

Fig. 8. The influence of inter-particle friction μ_s on the small strain stiffness behaviour: *(a)* G_0 , (b) γ_e , (c) γ_r , (d) m.

$$\sigma_{ij}^{c} = \frac{2}{5}\sigma^{0}A_{ij}^{c} \tag{16}$$

$$\sigma_{ij}^{b} = \frac{2}{5}\sigma^{0}A_{ij}^{b} \tag{17a}$$

$$A_{ij}^{b} = \frac{2}{5}\left(A_{ij}^{b_n} + \frac{3}{2}A_{ij}^{b_t}\right) \tag{17b}$$

$$\sigma_{ij}^{f} = \frac{2}{5}\sigma^{0}A_{ij}^{f} \tag{18a}$$

$$A_{ij}^{f} = \frac{2}{5}\left(A_{ij}^{f_n} + \frac{3}{2}A_{ij}^{f_t}\right) \tag{18b}$$

Consequently, the stress tensor can be expressed as:

$$\sigma_{ij} = \frac{N\overline{f}_0^{\mathrm{n}}\overline{b}_0^{\mathrm{n}}}{V}\left[\delta_{ij} + \frac{2}{5}A_{ij}^{c} + \frac{2}{5}\left(A_{ij}^{b_n} + \frac{3}{2}A_{ij}^{b_t}\right) + \frac{2}{5}\left(A_{ij}^{f_n} + \frac{3}{2}A_{ij}^{f_t}\right)\right] \tag{19}$$

Eq. (19) is known as the SFF relationship. Now, the only remaining unknown part is the calculation of each anisotropy tensor in Eq. (19), which is provided in Table 2.

The first column of Table 2 lists the distribution function represented by the anisotropy tensors, while the second column gives the calculation or definition of these tensors. The computation of the anisotropy tensors is straightforward. The symbols used in Table 2 are defined as follows: f^{n}, f^{t} in Eq. (T6) and Eq. (T10) denote the magnitudes of the normal contact force and tangential contact force, respectively, while b^{n}, b^{t} in Eq. (T13) and Eq. (T17) represent the magnitudes of the normal branch vector and tangential branch vector. It is noteworthy that $\overline{f}_0^{\mathrm{n}}$ and $\overline{b}_0^{\mathrm{n}}$ are a measure of the mean normal force and the mean normal branch vector in the assembly, respectively, which may differ from those derived by averaging over all contacts (Guo and Zhao, 2013; Ouadfel and Rothenburg, 2001; Sufian et al., 2017).

3.2. *Stress ratio-anisotropy relationship and stiffness-anisotropy relationship*

The term "stress ratio-anisotropy relationship" is first introduced by Ouadfel and Rothenburg (2001), to describe the exact relationship between stress ratio and the invariants of anisotropy tensor. Similarly, in this study, the term "stiffness-anisotropy relationship" is used to describe the relationship between stiffness and the contribution from the invariants of anisotropy tensor. Following is the key derivation process.

To quantify the degree of anisotropy of each anisotropy tensor, the second invariant of the anisotropy tensor is introduced:

$$a_{[*]} = \sqrt{\frac{3}{2}A_{ij}^{[*]}A_{ij}^{[*]}} \tag{20}$$

Here, the notation [*] represents the script c, b_n, b_t, f_n, f_t of each anisotropy tensor. In the triaxial condition, the calculation can be simplified as: $a_{[*]} = A_{11} - (A_{22} + A_{33})/2$, where A_11, A_{22}, and A_{33} are the diagonal elements of the tensor. Similarly, the mean effective stress p' and deviatoric stress q of the stress tensor is given by $p' = \sigma_{ii}$ and $q = \sqrt{3/2\sigma_{ij}\sigma_{ij}}$. In triaxial condition ($\sigma_2 = \sigma_3$), the q is taken as $q = \sigma_1 - \sigma_3$.

Based on Eq. (19) and Eq. (20), a relationship between stress ratio (η) and the term involving the second invariant of the anisotropy tensor can be established:

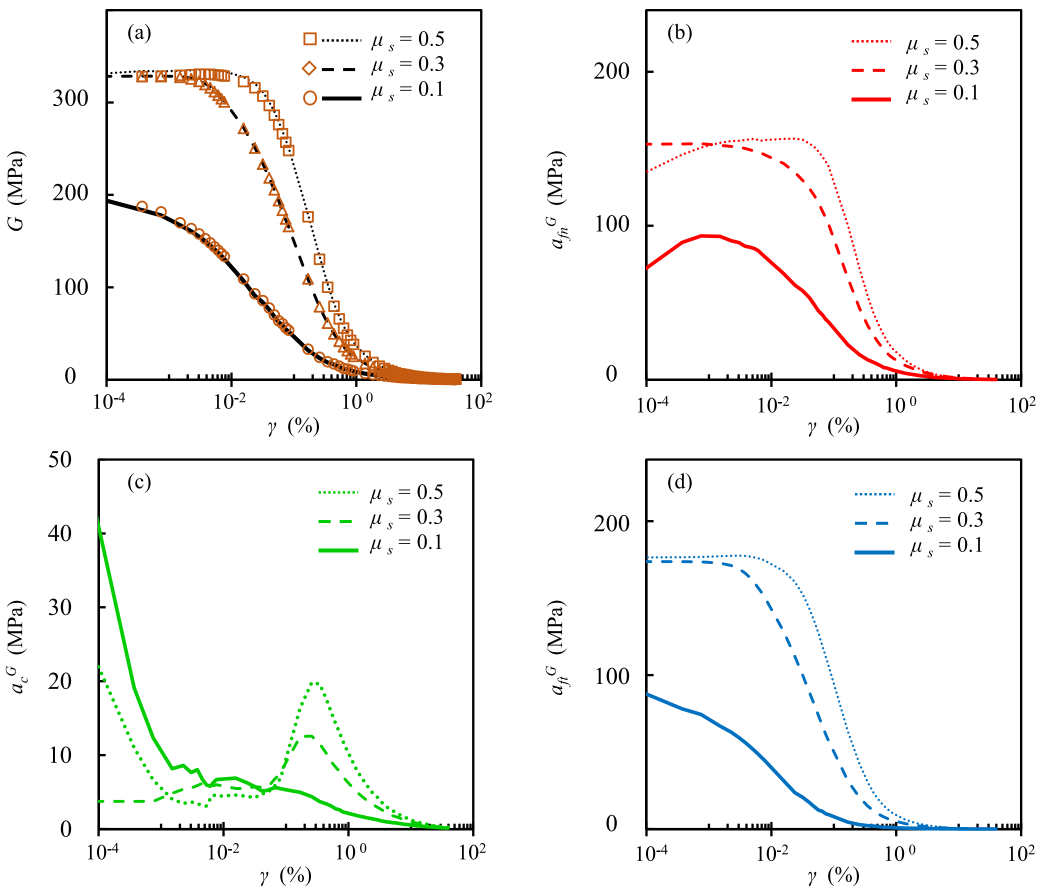

Fig. 9. The influence of inter-particle friction μ_s on the contribution from each anisotropy source to the small strain stiffness at $p_0{}' = 0.3$ MPa: (a) overall DEM result (marker) and SFF result (line), (b) $a_{f_n}^G$, (c) a_c^G, (d) $a_{f_t}^G$.

$$\eta = \frac{q}{p^{'}} = \frac{2}{5}\left(a_c - a_{b_n} - \frac{3}{2}a_{b_t} + a_{f_n} + \frac{3}{2}a_{f_t}\right) \tag{21}$$

The negative sign associated with the branch vector anisotropy is suggested by Ouadfel and Rothenburg (2001). For conciseness, the coefficient and the second invariant can be represented by a single term, yielding a more compact relationship between the stress ratio and the invariants of the anisotropy tensor:

$$\eta = \frac{q}{p^{'}} = a_c^{\eta} + a_{b_n}^{\eta} + a_{b_t}^{\eta} + a_{f_n}^{\eta} + a_{f_t}^{\eta} = a^{\eta} \tag{22}$$

Here, a^{η} on the right side of Eq. (22) denotes the sum of the second invariant related term of the anisotropy tensor, a_c^{η}, $a_{b_n}^{\eta}$, $a_{b_t}^{\eta}$, $a_{f_n}^{\eta}$, $a_{f_t}^{\eta}$, which represents the contribution of contact normal, normal and tangential branch vector, normal and tangential forces to the stress ratio, respectively.

Following a similar approach in Eq. (22), the "stiffness-anisotropy relationship" is proposed in this study to investigates the contribution of anisotropy source to the stiffness, quantified by the secant shear modulus, defined as $G_{sec} = q/3\varepsilon_q$, where $\varepsilon_q = 2/3(\varepsilon_1 - \varepsilon_3)$ is the deviatoric strain. By multiplying p' on both sides of Eq. (22), it is straightforward to establish the relationship between total deviatoric stress and the stress component from each anisotropy, which can be expressed as:

$$q = a_c^{q} + a_{b_n}^{q} + a_{b_t}^{q} + a_{f_n}^{q} + a_{f_t}^{q} = a^{q} \tag{23}$$

Obviously, the terms are given by $a_{[*]}^{q} = p'a_{[*]}^{\eta}$. Subsequently, by dividing the deviatoric strain on both sides of Eq. (23), one can deduce the relationship between the secant shear modulus and each anisotropy component, i.e., "stiffness-anisotropy relationship":

$$G_{sec} = a_c^{G} + a_{b_n}^{G} + a_{b_t}^{G} + a_{f_n}^{G} + a_{f_t}^{G} = a^{G} \tag{24}$$

Hence, the term $a_{[*]}^{G} = a_{[*]}^{q}/3\varepsilon_q$, represents the contribution of each anisotropy component to the stiffness. Through the application of Eq. (22) and Eq. (24), this study can explore the contribution from different forms of anisotropy sources at both small (i.e., a_c^G, $a_{b_n}^G$, $a_{b_t}^G$, $a_{f_n}^G$, $a_{f_t}^G$) and large strains (i.e., a_c^{η}, $a_{b_n}^{\eta}$, $a_{b_t}^{\eta}$, $a_{f_n}^{\eta}$, $a_{f_t}^{\eta}$).

3.3. Validation of the SFF and typical SFF results at large and small strains

To validate the SFF relationship employed in this study, the stress ratio (a^{η}) based on Eq. (22) is plotted against the stress ratio (η) obtained from typical DEM simulations (reference cases in Table. 1) with different confining pressures, as depicted in Fig. 2, with the 1:1 dashed line signifying $a^{\eta} = \eta$. A good linear correlation is observed between the SFF-based stress ratio and measured stress ratio, indicating that the simplified SFF relationship, which omits some high-order terms Eq. (12b), is reasonable in this study.

The typical SFF relationship at small strain and large strain are presented in Fig. 3a and 3b, respectively. At large strains (Fig. 3a), the anisotropy components associated with contact force ($a_{f_n}^{\eta}$ and $a_{f_t}^{\eta}$) rapidly increase to a peak and then gradually decrease to a steady value. The branch vector-related components ($a_{b_n}^{\eta}$ and $a_{b_t}^{\eta}$) demonstrate a negative impact on the stress ratio, consistent with the previous studies (Ouadfel and Rothenburg, 2001; Zhao et al., 2018). The contact normal term (a_c^{η}) exhibits a more gradual increase to a steady value. At sufficiently large strain (critical state or steady state), the anisotropy from normal force

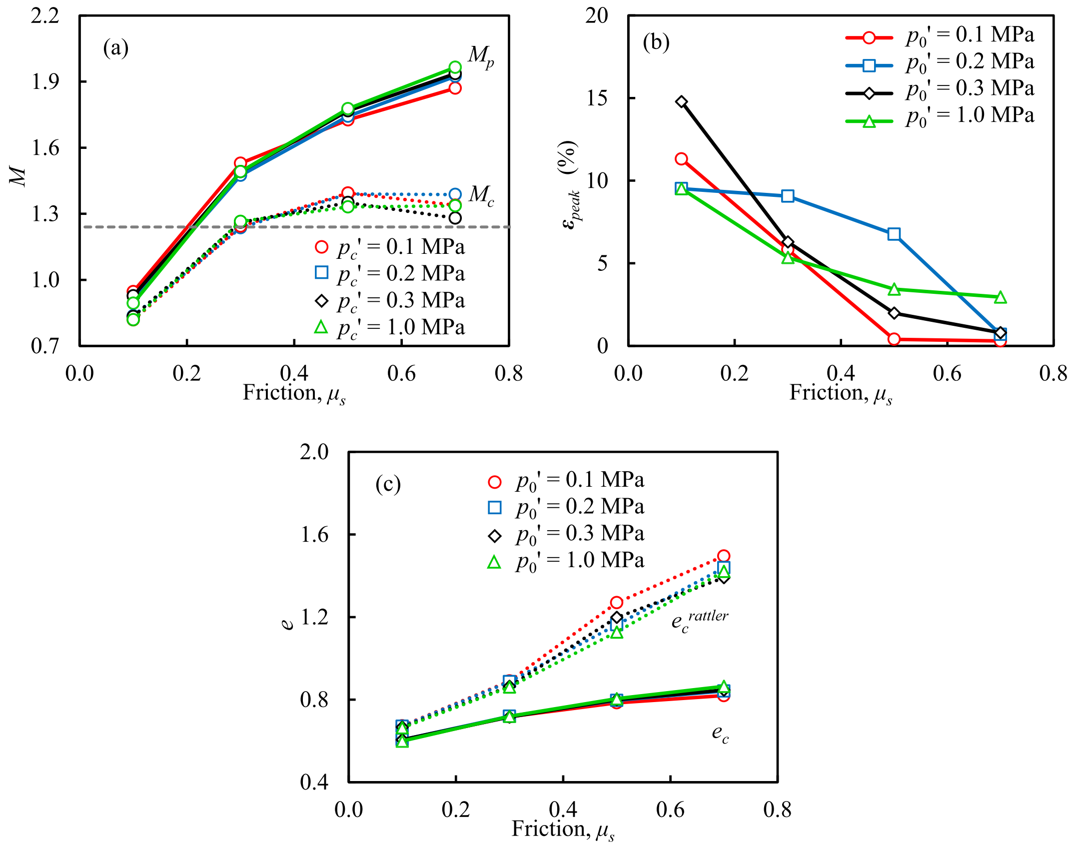

Fig. 10. The influence of inter-particle friction μ_s on the large-strain behaviour: (a) M_p (solid line) and M_c (dash line); (b) $\varepsilon_{\text{peak}}$; (c) e_c (solid line) and e_c^{rattler} (dash line).

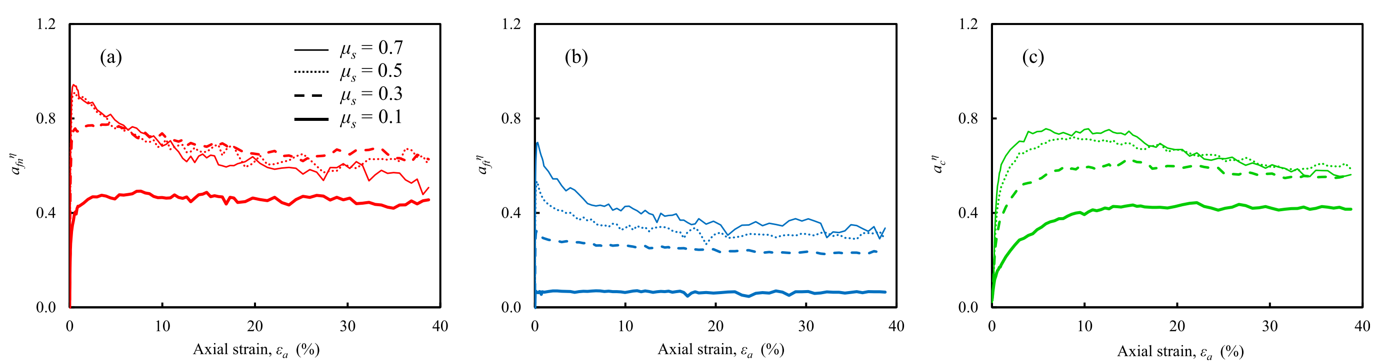

Fig. 11. The influence of inter-particle friction μ_s on the anisotropy behavior at large strains ($p_0{}' = 0.3$ MPa): (a) $a_{f_n}^{\eta}$; (b) $a_{f_t}^{\eta}$; and (c) a_c^{η}.

($a_{f_n}^{\eta}$) emerges as the primary contributor to the strength, followed by the contact normal (a_c^{η}), and then the tangential force ($a_{f_t}^{\eta}$), with the tangential and normal branch vector ($a_{b_t}^{\eta}$ and $a_{b_n}^{\eta}$) contributing negatively and minimally.

At small strains (Fig. 3b), only the contact force anisotropy component contributes to the stiffness and its degradation. Initially, the tangential contact force ($a_{f_t}^{G}$) has a steady positive contribution to the stiffness, but a significant decline follows this. Similarly, the normal force component ($a_{f_n}^{G}$) also sustains a steady positive contribution before significantly decreasing. Within the small strain range, neither the contact normal (a_c^{G}) nor the branch vector ($a_{b_n}^{G}$ and $a_{b_t}^{G}$) obviously influences stiffness and its degradation, although the contact normal is the second important contributor to the strength at large strains.

Another interesting observation in Fig. 3b is that the contribution from tangential force ($a_{f_t}^{G}$) to maximum shear modulus is slightly larger than that from normal force ($a_{f_n}^{G}$), and the degradation rate of tangential force is faster than normal forces. Moreover, the degradation of the tangential force and normal force occurs near the elastic strain threshold (where shear modulus started to decrease), which may signal the onset of (obvious) inter-particle sliding (Nguyen, 2022; Zhou and Xu, 2024).

Recent research (Zhou and Xu, 2024) highlighted the importance of an evident increase in the contact normal anisotropy for the stiffness degradation mechanism. They compared the evolution of contact normal anisotropy directly with the stiffness degradation curve rather than computing the contribution of the contact normal, as done in this study. However, this study suggests that contact force anisotropy is the most significant factor controlling stiffness degradation. More critically, results in Fig. 3b revealed that the contact normal has a negligible contribution to both stiffness and its degradation at small strains despite

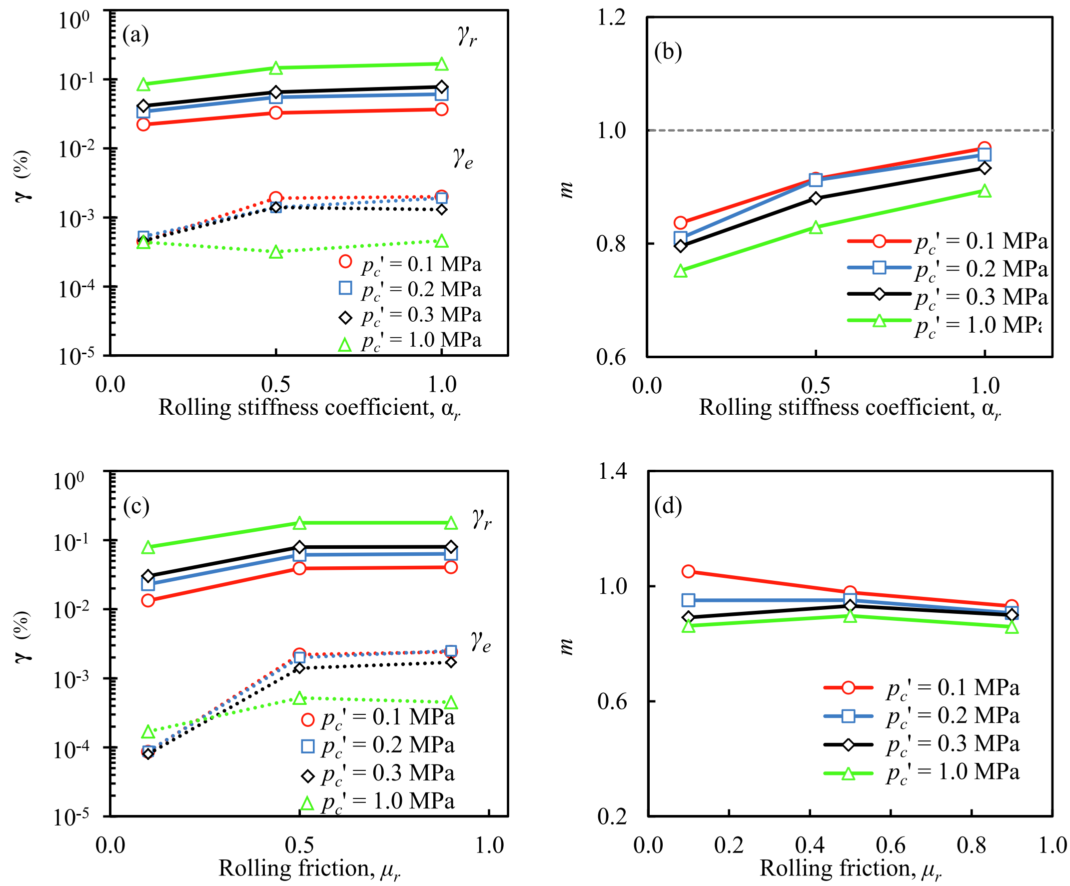

Fig. 12. The influence of rolling stiffness coefficient α_r on (a) γ_e and γ_r , (b) m; and influence of rolling friction μ_r on (c) γ_e and γ_r , (d) m.

a small peak near the elastic strain threshold observed. Considering the SFF at small strains reproduces the stiffness degradation curve with satisfactory accuracy, as same as its good precision at larger strains, analysis in this study using SFF may be more demonstrated in explaining the mechanism of small strain stiffness and its degradation.

The findings on anisotropy sources in this study are based on a simple clump-based shape model. However, these findings should remain qualitatively generalizable when employing other particle shape modelling approaches. Many studies have utilized different modeling methods, such as, super-ellipsoid (Zhao et al., 2018; Zhao and Zhou, 2017), polyhedral (Azéma et al., 2013), and clump models (Gong and Liu, 2017). These studies consistently demonstrated conclusions similar to those in this study at large strains: contribution from normal force anisotropy is dominated, followed by contact normal and tangential forces, with the normal and tangential branch vectors being negative and minimal. This study is the first one to apply the SFF relationship at small strains, and thus, there are no existing studies for direct comparison. Nevertheless, given the consistent results observed at large strains across various particle shapes modelling algorithms, it is reasonable to infer that our findings at small strains are also generalisable.

4. Macro behaviour and the micro mechanism

4.1. Quantitative description of macro behavior at small strain and large strain

To quantitatively describe the macro behaviour of granular material at small and large strains, the secant stiffness degradation curve ($G_{\text{sec}} - \gamma$), the stress–strain ($\eta - \varepsilon_a$) relationship and the void ratio-strain relationship ($e - \varepsilon_a$) are determined. And several key parameters that determine the properties of these curves are selected to describe the behaviour of granular materials in different strain ranges.

For small-strain behaviour, a hyperbolic stiffness degradation model proposed by Oztoprak and Bolton (2013) was employed to fit the $G_{\text{sec}} - \gamma$ curve:

$$G_{\text{sec}} = G_0 \Big/ \left(1 + \left[\frac{\gamma - \gamma_e}{\gamma_r}\right]^m\right) \tag{25}$$

where G_{sec} is the secant shear modulus; G_0 is the maximum (elastic) shear modulus at a very small strain; γ_e is the elastic strain threshold below which soil stiffness starts to reduce with increasing strain; γ_r is the reference shear strain (strain at G_{sec} / G_0 = 0.5); m is the curvature parameter. The last two parameters govern the degradation rate of stiffness.

For large-strain behaviour, the peak stress ratio M_p and its corresponding axial strain $\varepsilon_{\text{peak}}$, the critical state stress ratio M_c (the stress ratio at the maximum axial strain ~ 40 %) is used to describe the η-ε_a curve, the critical state void ratio e_c and critical state effective void ratio e_c^{rattler} is selected for the $e - \varepsilon_a$ curve. The calculation of the effective void ratio does not consider rattlers (particles with only one or zero contacts) as part of the void space, while the void ratio does.

The parameters presented above provide a comprehensive description of the material's macro response under different strain conditions, while the characterization of micro-anisotropy sources is detailed in Section 3. For the sake of brevity, only the dominant micro-anisotropy component is analysed, while the tangential and normal branch vector contribute negatively and minimally in all cases and thus will be neglected in the following analysis. Table 3 summarise the variable describing the macro response feature and micro anisotropy source at small and large strains.

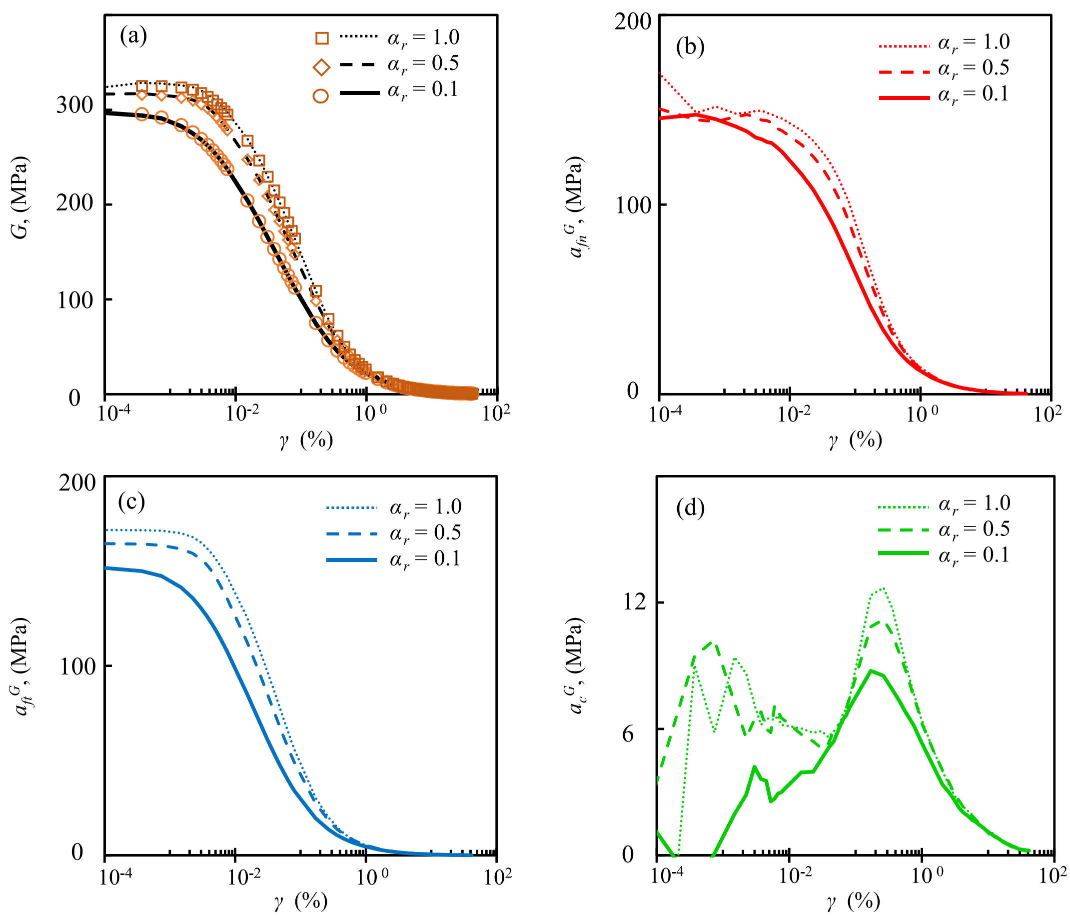

Fig. 13. The influence of rolling stiffness coefficient α_r on the contribution from each anisotropy source to the small strain stiffness at $p_0{}' = 0.3$ MPa: (a) overall DEM result (marker) and SFF result (line); (b) a_{fn}^G; (c) a_{ft}^G; (c) a_c^G.

4.2. Effects of particle Young's modulus on macro–micro behaviour

Fig. 4 and Fig. 5 present the relationship between particle Young's modulus (E_p) and the stiffness parameters (G_0, γ_e, γ_r and m), as well as the contribution of each anisotropy source (a_c^G, a_{fn}^G, a_{ft}^G) to the stiffness under different E_p values.

As shown in Fig. 4a, G0 increases almost linearly with the increase of E_p on a logarithmic scale. This observation could be explained by the theory proposed by Chang and Liao (1994) for randomly packed spheres: $G_0 = \frac{Z_m k_n}{4\pi R(1+e)}\left(\frac{5k_t}{3k_n+2k_t}\right)$, where Z_m is the mechanical or effective coordination number. This equation shows that the normal contact stiffness G_0 is proportional to k_n. Based on Eq. (4), k_n has a linear relationship with E_p if other parameters remain unchanged. Thus, the increase of G_0 should be proportional to the E_p if all other conditions remain constant. Gong et al. (2024) have studied the effect of particle modulus on G_0 and also reported that the G_0 is solely dependent on mechanical coordination number and contact stiffness. Furthermore, Fig. 5a shows how anisotropy components contribute to the increase of G_0 with increasing E_p. The maximum values of mechanical anisotropy a_{fn}^G and a_{ft}^G increase with E_p and remain the dominant contributors to G_0. This may be attributed to the influence of contact stiffness on the magnitude of contact forces (as shown in Eqs. (4–5)). An increase in E_p enhances the contact stiffness, thereby increasing the magnitude of contact forces. Consequently, as described in Eqs. (T6) and (T10), this leads to an increase in mechanical anisotropy at the small strain range, where the structure of the contact network may not change significantly. Interestingly, the contact normal also increases with E_p, although its contribution to G_0 remains negligible.

Fig. 4b, c and d demonstrate that the γ_e , γ_r , and m decrease with the increase of E_p . The decrease in γ_r is almost linear on the log–log axis. The change in degradation rate (m) and onset (γ_e , γ_r) could be explained using the SFF relationship, as shown in Fig. 5b, 5c and 5d. The degradation of a_{fn}^G and a_{ft}^G becomes earlier with higher E_p . The degradation of a_c^G also occurs earlier, although it has a minimal effect on the G_0.

The influence of E_p on the large-strain behaviour at both the macro (Fig. 6) and micro scales (Fig. 7) is presented. As shown in Fig. 6a and 6b, M_c remains constant with increasing E_p. In contrast, M_p exhibits a slight increase, and ε_{peak} has a small decrease as E_p increases from 0.7 to 7 GPa, beyond which they remain nearly constant up to 70 GPa. From a micromechanics perspective (Fig. 7), an increase in E_p accelerates the increase rate of all anisotropy components ($a_{[*]}^{\eta}$) at the beginning of the shearing, resulting in the anisotropy sources in specimens with higher E_p reaching the peak or steady value more rapidly (i.e., ε_{peak} decrease). Concurrently, the increase of E_p raises the peak of a_{fn}^{η}, which causes the increase of M_p in the specimens. However, the steady value of each anisotropy component remains constant, and thus M_c is unchanged.

Fig. 6c suggests that both e_c and $e_c^{rattler}$ increase with increasing E_p. Besides, an important observation is that the increase of E_p eliminates the influence of the mean effective stress p' on the two critical state void ratios (e_c and $e_c^{rattler}$). That is, in low E_p ($< \sim 10$ GPa), e_c and $e_c^{rattler}$ decreases with the p', which is similar to the actual sand's response (Verdugo and Ishihara, 1996). However, in high E_p ($> \sim 10$ GPa), e_c and $e_c^{rattler}$ remains almost identical (more obvious in e_c) under different mean effective stress. Additionally, the difference between the e_c and $e_c^{rattler}$ become larger with the increase of E_p. Although a high E_p value is

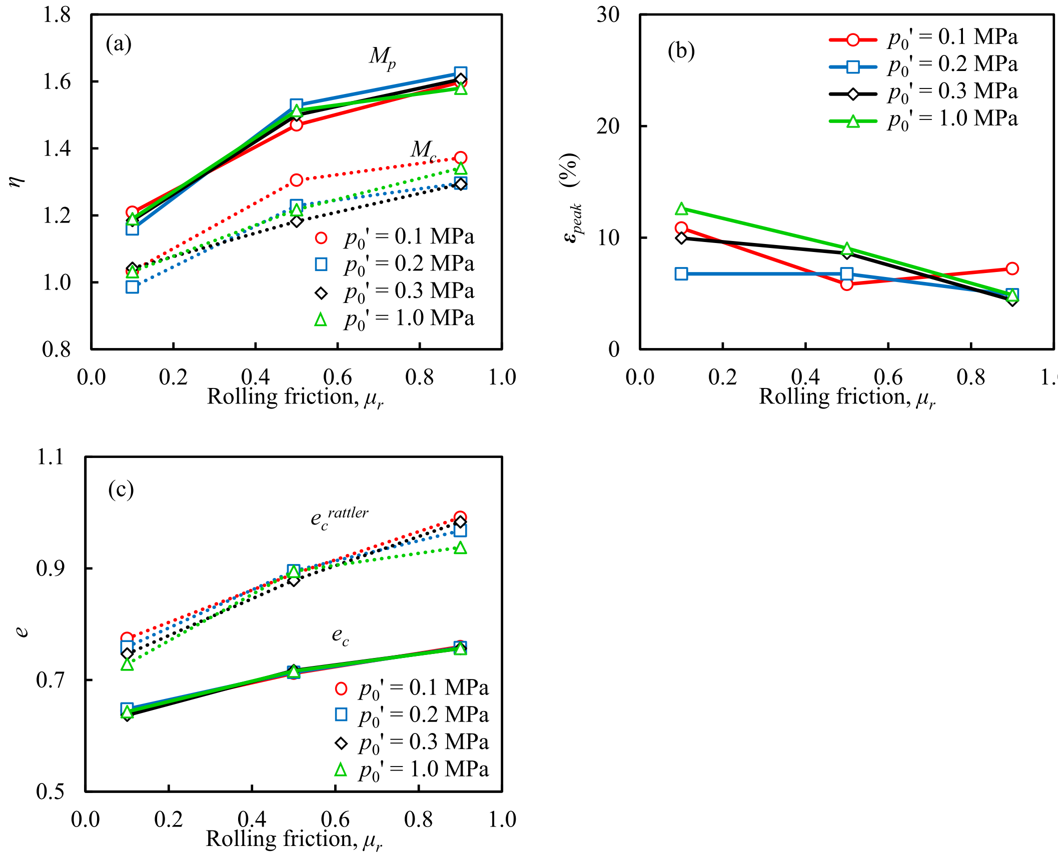

Fig. 14. The influence of μ_r on the large-strain behaviour: (a) M_p (solid line) and M_c (dash line); (b) $\varepsilon_{\text{peak}}$; (c) e_c (solid line) and e_c^{rattler} (dash line).

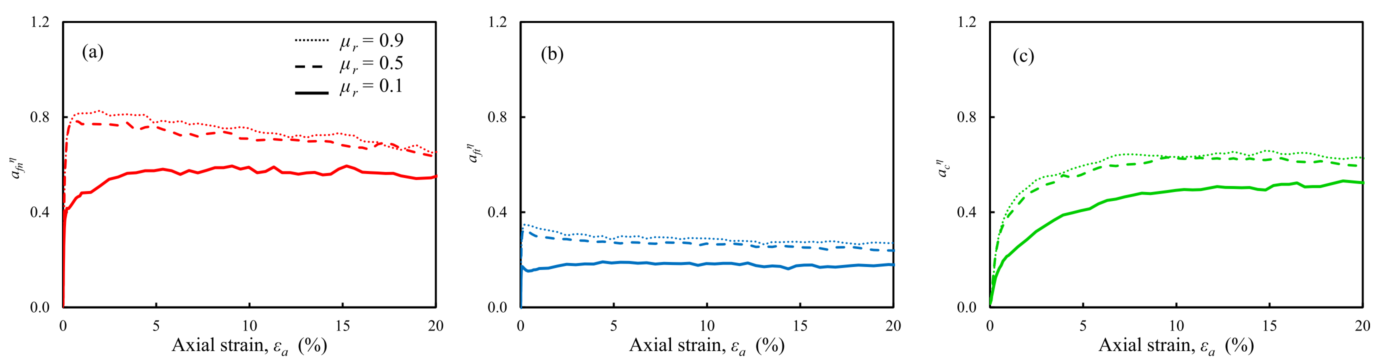

Fig. 15. The influence of rolling friction μ_r on the anisotropy behaviour at large strains ($p_0{}' = 0.3$ MPa): (a) $a_{f_n}^{\eta}$; (b) $a_{f_t}^{\eta}$; and (c) a_c^{η}.

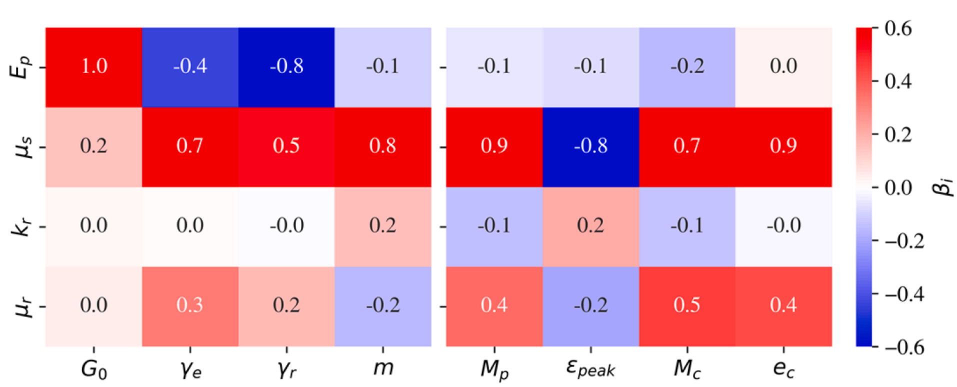

	G_0	γ_e	γ_r	m	M_p	ε_{peak}	M_c	e_c
E_p	1.0	-0.4	-0.8	-0.1	-0.1	-0.1	-0.2	0.0
μ_s	0.2	0.7	0.5	0.8	0.9	-0.8	0.7	0.9
k_r	0.0	0.0	-0.0	0.2	-0.1	0.2	-0.1	-0.0
μ_r	0.0	0.3	0.2	-0.2	0.4	-0.2	0.5	0.4

Fig. 16. The importance of micro contact parameter on the macro feature at both small and large strains.

necessary to achieve reasonable G_0 (around 100 ~ 500 MPa for the stress level and void ratio in this study), it comes at the cost of sacrificing some important aspects or features of large-strain behaviour, such as the p'-dependent critical state void ratio (e_c and e_c^{rattler}).

4.3. Effects of inter-particle friction on macro–micro behaviour

Fig. 8 and Fig. 9 illustrate the influence of inter-particle friction (μ_s) on small-strain behaviour at both macro and micro scales. As shown in Fig. 8a, G_0 remains unaffected by μ_s when μ_s exceeds 0.3, a finding that aligns with the observations reported by Reddy et al. (2022). This independence of G_0 on μ_s can be further explained by the micro anisotropy analysis in Fig. 9b and 9d, which shows that the contribution from contact force ($a_{f_n}^G$ and $a_{f_t}^G$) also remains unchanged with increasing μ_s for $\mu_s > 0.3$.

Fig. 8b-d shows that the γ_e, γ_r, and m exhibit a decrease as μ_s decreases, indicating that μ_s governs the onset and rate of stiffness degradation. At the micro-scale (Fig. 9b and 9d), the “elastic strain” of $a_{f_n}^G$ and $a_{f_t}^G$ (i.e., the shear strain at which the contribution from anisotropy sources starts to drop) shifts to the left, which means their degradation is advanced. This result explains the observation that γ_r and γ_e decreases with decreasing μ_s. The advanced degradation of anisotropy may be attributed to the increased instability in the contact network, which is induced by a decrease in μ_s. This decrease in μ_s makes it easier for the contact network to adjust its structure. For the contact normal (Fig. 9c), its peak (at $\gamma \sim 1$ %) significantly decreases with the decrease of μ_s. However, its overall contribution remains negligible. An interesting observation is that the shear strain at which a_c^G reaches peak is unaffected by μ_s.

The above paragraphs analyse the influence of μ_s on the small-strain behaviour and the micro mechanism. In the following, the goal is to compare these stiffness parameters (G_0, γ_e, γ_r and m) with those observed results in real quart sand and then determine a suitable range for small-strain behaviour modelling. According to the database compiled by Oztoprak and Bolton (2013), γ_r ranges from 0.02 to 0.1 %, while γ_e ranges from 0 to 0.003 %. The typical values of m are 0.75 to 1.0 (the upper bound is plotted as dashed lines in Fig. 8b-d). Fig. 8 shows that with μ_s varying from 0.1 to 0.3, the γ_e remains below approximately 0.004 %, and γ_r falls within 0.01 % to 0.4 %, the curvature parameter (m) varies from 0.65 to 1.00, similar to the range observed in real soil.

Furthermore, it is also essential to directly compare the measured inter-particle friction of granular materials with that used in this study. Sandeep et al. (2018) measured the friction of glass beads and quartz sand (Leighton Buzzard sand), with typical value ranging from 0.10 to 0.23. When selecting friction within this range, the output in this study can fall within the typical parameter range of soil’s small strain stiffness response. Hence, employing the Hertz model and considering the typical E_p of quartz used in this study (~70 GPa), it is suggested that a reasonable selection range for μ_s is between 0.1–0.3 for quartz sand for small-strain behaviour.

Fig. 10 and Fig. 11 show the macro–micro behaviour of material at large strains under different μ_s. Fig. 10a indicates that both M_c and M_p exhibit a significant increase as μ_s increases. Concurrently, the disparity between M_p and M_c becomes larger with an increase in μ_s. The increase rate of M_p and M_c slows down with higher μ_s values, and the increase rate of M_c approaches near zero when μ_s exceeds a value of 0.3. Similar results have also been reported by Huang et al. (2014), although they did not consider the rolling friction in their simulation. This change in increase rate can be attributed to the fixed rolling friction (μ_r). A previous study (Wensrich and Katterfeld, 2012) has demonstrated that the angle of repose is controlled by both rolling and shearing friction, such that when these two frictions are significantly different, the influences of further increases in the larger friction parameter are negligible. From the perspective of micro anisotropy sources (Fig. 11), the increase in both M_c and M_p with increasing μ_s is contributed by each form of anisotropy source. The increase in $a_{f_n}^{\eta}$, $a_{f_t}^{\eta}$ and a_c^{η} at the critical state becomes negligible when μ_s exceed 0.3. This observation is consistent with the results that the influences of further increases in μ_s are negligible to M_c when μ_s is larger than 0.3. Meanwhile, when μ_s exceeds 0.3, the increase of $a_{f_n}^{\eta}$ at the peak state becomes negligible. However, $a_{f_t}^{\eta}$ still has a considerable rise, so M_p can still increase, but at a lower rate.

In contrast to the trends observed in γ_e and γ_r, Fig. 10b shows that $\varepsilon_{\mathrm{peak}}$ decreases with increasing μ_s. It should be noted that when μ_s is small (< 0.3), $\varepsilon_{\mathrm{peak}}$ is quite large. This finding can be attributed to the fact that the higher μ_s led to a larger maximum void ratio, thereby enhancing the specimen’s relative density (despite the specimen having almost the same void ratio before shearing). In other words, when μ_s is small, the response of the specimen is strain-hardening and has no peak stress ratio, so $\varepsilon_{\mathrm{peak}}$ represents the strain at which the shearing ends. As μ_s exceeds 0.3, the response of material transitions from strain-hardening (loose sand) to strain-softening (dense sand), leading to a significant decrease in $\varepsilon_{\mathrm{peak}}$. In the strain-softening cases, $\varepsilon_{\mathrm{peak}}$ shows a slight decrease with increasing μ_s. Fig. 10c shows that both e_c and e_c^{rattler} exhibit a nearly linear increase in response to increasing μ_s. However, the dependence of e on effective pressure cannot be modelled well. Although a detailed exploration of this behaviour is beyond the scope of this study, it is a valuable topic for future research.

In the following, the computed strength is compared with experimental results obtained from quartz sand. According to experimental database of sand (Andersen and Schjetne, 2013), the typical lower bound value for M_c in quartz sand is 1.24 (grey dash line in Fig. 10a). As shown in Fig. 10a, when μ_s exceeds 0.3, the computed M_c values would larger than this lower bound, aligning well with the experimental findings. Additionally, the computed M_p increases from 1.5 as μ_s increase from 0.3, which falls within the reasonable range observed in experiments (Andersen and Schjetne, 2013), approximately from 1.5 to 1.8 for dense sand ($D_r > 80$ %). However, the pressure dependence of M_p is not captured by the current model.

Based on these comparisons, it can be concluded that a μ_s value of at least 0.3 is required to accurately reproduce the strength feature for large-strain behaviour. However, this value differs significantly from the optimal value for simulating small-strain behaviour (0.1–0.3). One possible explanation for this discrepancy is that the simple particle shape adopted in this study underestimates the interlocking between particles during dilation.

4.4. Effects of rolling stiffness and rolling friction on macro–micro behaviour

The influence of the two rolling stiffness parameters (α_r and μ_r) on stiffness behaviour and anisotropy is an important aspect of this study. As depicted in Fig. 12., the change in α_r would affect the stiffness degradation rate and onset. That is, the increase in α_r leads to increases in the γ_e, γ_r and m. On the other hand, μ_r also accelerates stiffness degradation rate (an elevated μ_r increases γ_r and γ_e), but its effects on m are relatively minor. As for G_0, both α_r and μ_r have negligible effects on it and thus are not shown.

Fig. 13 demonstrates the influence of α_r on the contribution from each anisotropy source to the small-strain behaviour. As α_r increase, the contribution from $a_{f_t}^G$ (Fig. 13b) and $a_{f_n}^G$ (Fig. 13c) but remain largely unchanged. Conversely, the “elastic strain” of $a_{f_n}^G$ and $a_{f_t}^G$ decreases with decreasing α_r, resulting in a flatter curve shape for degradation. This observation is consistent with the decrease in γ_e, γ_r and m with decreasing α_r, due to the fact that decreased rolling resistance would reduce particle “inter-locking”, thereby accelerating deformation and slippage within the contact network. Given that the influence of μ_r on the anisotropy contribution is similar to that of α_r (primarily affecting the shape of the stiffness-anisotropy curve), the results for μ_r are not presented here for the sake of simplicity, as they do not provide additional insights beyond those obtained from the α_r analysis.

Regarding large-strain behaviour (Fig. 14), an increase in μ_r exhibits a similar effect to that of μ_s, whereas the change in α_r has a very small influence on large strain response and is therefore not shown. Fig. 14 demonstrates that an increase in μ_r enhances the strength (both M_c and M_p) and increases the critical state void ratio (e_c and e_c^{rattler}), while the $\varepsilon_{\text{peak}}$ shows a slight decreasing trend. Additionally, the increase in strength caused by μ_r becomes slower with larger μ_r, which is attributed to the fixed value of μ_s, as discussed in Section 4.2.

Fig. 15 illustrates the evolution of each anisotropy source at large strains under different μ_r. The increase of strength, induced by μ_r, is also a collective contribution from the increase in each form of anisotropy components (a_c^η, $a_{f_n}^\eta$ and $a_{f_t}^\eta$). The increase in M_p with increasing μ_r is primarily attributed to the increase of force anisotropy, which response changes from hardening to softening (a peak can be observed when $\mu_r >$ 0.1), as shown in Fig. 15a and Fig. 15b.

4.5. Sensitivity analysis of micro-contact parameters on macro features

The importance of micro-contact parameters on macro features is visualised through heat maps in Fig. 16. To quantify this importance relationship, a normalised linear multiple regression equation is employed:

$$Y_{\text{norm}} = \sum_{i=1}^{4} \beta_i X_i^{norm} + \beta_0 \quad (26)$$

where Y^{norm} represents the macro features at small strains (G_0, $\log[\gamma_e]$, $\log[\gamma_r]$ and m) and large strains (M_p, $\varepsilon_{\text{peak}}$, M_c and e_c), and X^{norm} denotes the micro-contact parameters (E_p, μ_s, μ_r and k_r). Both X^{norm} and Y^{norm} are normalised by standardization, i.e., each original value is normalised by subtracting the mean (average) value and then dividing by the standard deviation. Although this equation assumes a linear relationship between micro-contact parameters and macro features, which is not entirely accurate based on previous results, it serves as a simplified approach to demonstrate the sensitivity of macro features to different micro parameters. The absolute value of β_i indicates the relative importance of each micro-contact model parameter to the corresponding macro feature, with smaller values suggesting less importance or less dependence. The sign of β_i indicates whether there is a positive or negative correlation between the examined variables. It should be noted that although the data from only 100 kPa confining pressure is shown here as one example, the results from other stress levels exhibit similar trends.

The results clearly indicate that E_p is the most critical parameter controlling the maximum small-strain stiffness of the specimen, and it is also the primary parameter that controls the stiffness degradation rate and onset. However, E_p does not influence large-strain behaviour. In contrast, μ_s and μ_r have similar effects on both small- and large-strain behaviour, although the influence of μ_r is relatively smaller. At small strains, these two friction coefficients mainly influence the degradation rate and onset of stiffness, whereas at large strains, they substantially affect the strength (M_p, $\varepsilon_{\text{peak}}$, M_c) and dilation (e_c) of the specimen. The influence of α_r is smallest compared to other contact model parameters.

5. Conclusions

The parametric study reveals the quantitative relationship between local contact model parameters and the macro response. That is, the increase of maximum shear modulus is found to be strongly correlated with the increase of particle Young's modulus. The increase in critical state stress ratio and void ratio is induced by increasing shearing friction and rolling friction. Furthermore, the remaining macro characteristics, including stiffness degradation onset and rate, peak stress ratio and its corresponding axial strain, exhibit complex dependencies on multiple contact model parameters, including particle Young's modulus, shearing friction, and rolling stiffness.

The results of this study highlight the limitations of DEM simulations employing the well-established Hertz contact model alongside simple clump shape modelling. It is difficult to quantitatively capture both small-strain and large-strain behaviors for quartz sand using a single set of model parameters, such as the pressure dependence of critical state void ratio, even with careful parameter selection. However, this contact model can accurately capture the behaviour at either small strains or large strains. Hence, modellers should calibrate model parameters based on whether their focus is on large-strain or small-strain behaviour. It is also recommended that future research investigate the influence of particle shape, which is known to significantly influence both small and large-strain behaviour. By incorporating more realistic particle shape modelling, it is possible to capture the behaviour across the entire strain range.

The primary focus of this study is on the relative importance of each anisotropy source's contribution to strength and stiffness rather than their absolute changes. In this study, it is found that the relative importance of each anisotropy source is dependent on strain level rather than particle physical properties. That is, changes in contact model parameters always affect all forms of anisotropy at both small and large strains. However, these changes are consistent or proportional to each anisotropy source, thereby preserving the relative weight or importance between anisotropy sources.

At small strains, the most important anisotropy components are the contact forces, particularly tangential forces. Besides, the degradation of tangential force anisotropy is strongly related to the macro stiffness degradation, which may signal the onset of significant inter-particle sliding and evident mechanical stability change of contact network. In contrast, the contact normal contributes minimally to stiffness or its degradation, despite being the second most important contributor to strength at large strains. Changes in contact model parameters influence the mechanical anisotropy instead of geometric anisotropy, which in turn affects stiffness behaviour.

At large strains, all sources of anisotropy contribute to the material's strength: the normal force anisotropy has the highest contribution, followed by contact normal and tangential forces, the normal and tangential branch vector contribution are negative and minimal. Change of contact model parameters influence both the mechanical and geometric anisotropy to affect the strength.

CRediT authorship contribution statement

Qing Chen: Writing – original draft, Validation, Investigation, Formal analysis, Data curation. **Chao Zhou:** Writing – review & editing, Supervision, Funding acquisition, Formal analysis, Conceptualization.

Declaration of competing interest

The authors declare that they have no known competing financial interests or personal relationships that could have appeared to influence the work reported in this paper.

Acknowledgement

The authors would like to thank the Research Grants Council (RGC) of the HKSAR for providing financial support through grant N_PolyU526/23 and AoE/E-603/18. This work was also supported by RISUD/PolyU under Grant 1-BBWS.

Appendix

This section presents the results of two forms of the SFF relationship: one with a fixed negative sign and another with a changeable sign determined by the coaxiality quantity S_r. The SFF relationship with a fixed negative sign, as recommended by Ouadfel and Rothenburg (2001), is used in this study, i.e., Eqs. (20–21). Conversely, another form of the SFF relationship employs a changeable sign determined by the coaxiality quantity S_r, which is adopted by Guo and Zhao (2013):

$$a_{[*]} = sign(S_r)\sqrt{\frac{3}{2}A_{ij}^{[*]}A_{ij}^{[*]}} \tag{A.1}$$

$$S_r = A_{ij}^{[*]}\sigma_{ij}^{\text{dev}} \tag{A.2}$$

$$\eta = \frac{q}{p^{`}} = \frac{2}{5}\left(a_c + a_{b_n} + \frac{3}{2}a_{b_t} + a_{f_n} + \frac{3}{2}a_{f_t}\right) \tag{A.3}$$

Fig. A.1 compares the SFF results based on Eqs. (21) with those derived from Eqs. (A.3) for specimens composed of spheres. The SFF calculations using Eq. (21) and those based on Eq. (A.3) are almost identical, as the contribution from the branch vector is minimal. This finding is consistent with the report by Guo and Zhao (2013). However, in the case of non-spherical particles (Fig. A.2), the SFF relationship based on Eq. (A.3) tends to overestimate the stress ratio compared to the stress ratio calculated from Eq. (21), as the contribution from the branch vector becomes more significant, although still minor compared to other anisotropy sources. A similar result was also observed in the study by Zhao et al. (2018), where they found that the SFF relationship based on Eq. (A.3) tends to overestimate the stress ratio, while the complete form of SFF relationship using fixed negative sign achieves better consistency.

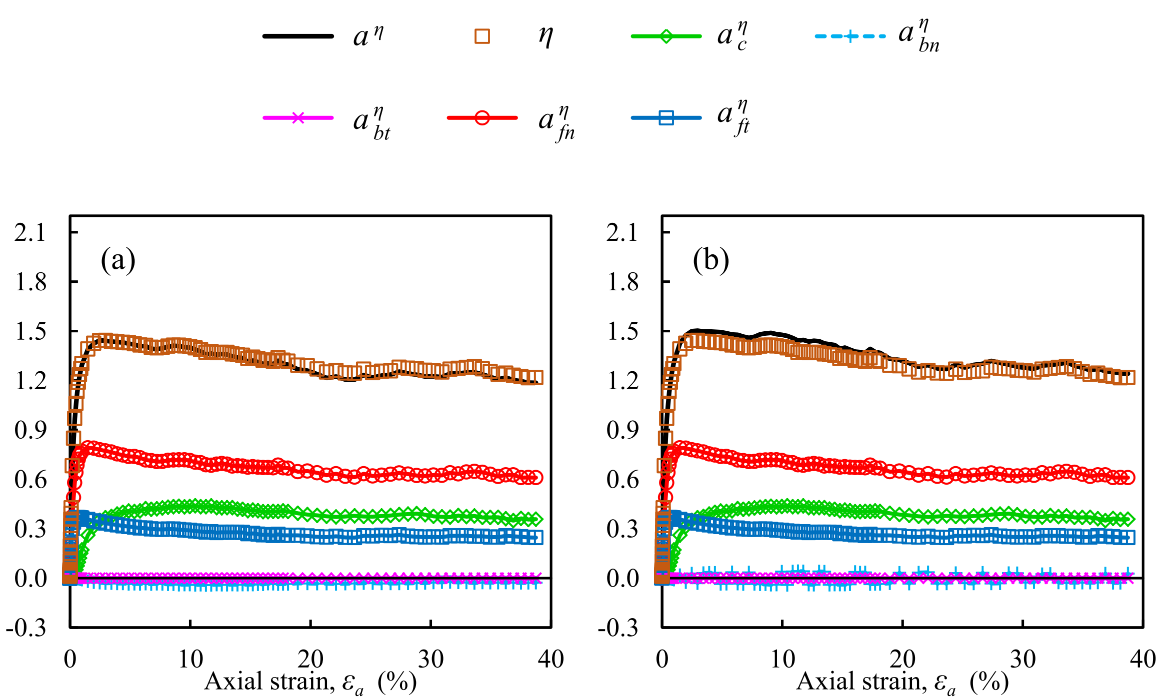

Fig. A1. SFF relationship (a) based on Eq. (21) and (b) based on Eq. (A.3) in a specimen consist of sphere.

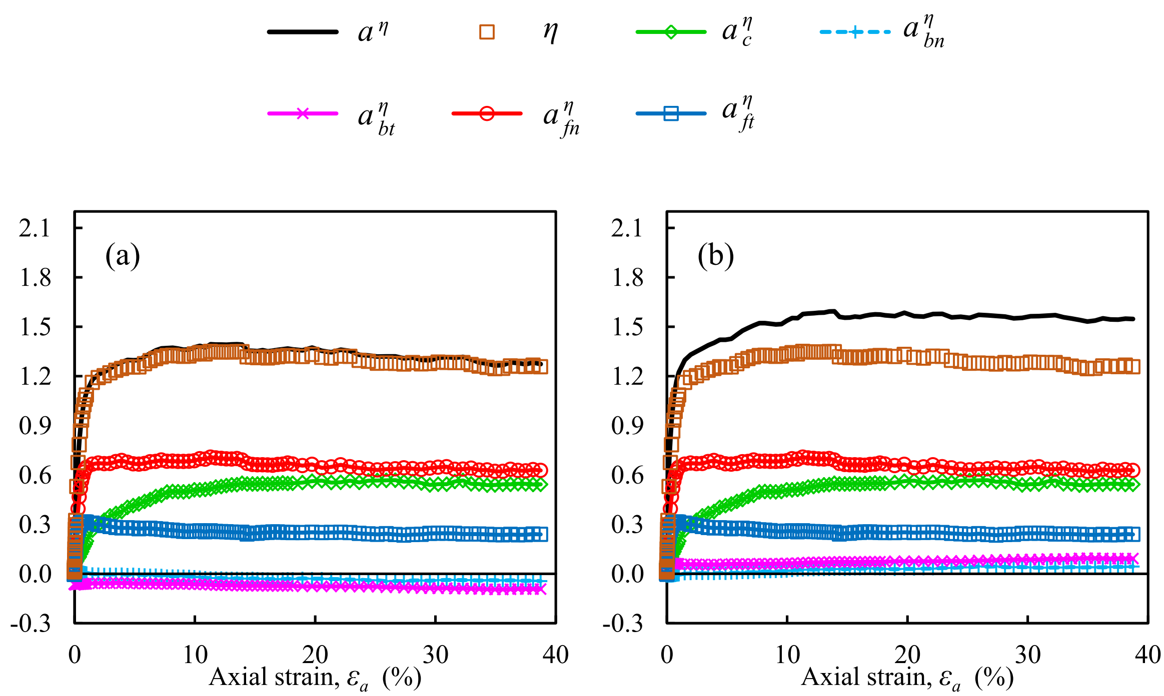

Fig. A2. SFF relationship (a) based on Eq. (21) and (b) based on Eq. (A.3) in a specimen consisting of clump particles used in this study.

Data availability

Data will be made available on request.

References

Altuhafi Fatin, N., Coop Matthew, R., Georgiannou Vasiliki, N., 2016. Effect of Particle Shape on the Mechanical Behavior of Natural Sands. Journal of Geotechnical and Geoenvironmental Engineering 142 (12), 04016071.
Andersen, K.H., Schjetne, K., 2013. Database of Friction Angles of Sand and Consolidation Characteristics of Sand, Silt, and Clay. Journal of Geotechnical and Geoenvironmental Engineering 139 (7), 1140–1155.
Antony, S.J., Kruyt, N.P., 2009. Role of interparticle friction and particle-scale elasticity in the shear-strength mechanism of three-dimensional granular media. Physical Review E 79 (3), 031308.
Atkinson, J., 2000. Non-linear soil stiffness in routine design. Géotechnique 50 (5), 487–508.
Azéma, E., Radjaï, F., 2010. Stress-strain behavior and geometrical properties of packings of elongated particles. Physical Review E 81 (5), 051304.
Azéma, E., Radjai, F., Dubois, F., 2013. Packings of irregular polyhedral particles: Strength, structure, and effects of angularity. Physical Review E—Statistical, Nonlinear, and Soft Matter. Physics 87 (6), 062203.
Belheine, N., Plassiard, J.P., Donzé, F.V., Darve, F., Seridi, A., 2009. Numerical simulation of drained triaxial test using 3D discrete element modeling. Computers and Geotechnics 36 (1–2), 320–331.
Bentil, O.T., Zhou, C., 2022. Effects of temperature and thermal cycles on the elastic shear modulus of saturated clay. Journal of Geotechnical and Geoenvironmental Engineering 148 (7), 06022006.
Bentil, O., Zhou, C., Zhang, J., Liu, K.K., 2023. Cross-anisotropic stiffness characteristics of a compacted lateritic clay from very small to large strains. Canadian Geotechnical Journal 60 (12), 1954–1967.
Bolton, M.D., 1986. The strength and dilatancy of sands. Géotechnique 36 (1), 65–78.
Chang, C.S., Liao, C.L., 1994. Estimates of Elastic Modulus for Media of Randomly Packed Granules. Applied mechanics reviews 47 (1S), S197–S206.
Cheng, Y.P., Bolton, M.D., Nakata, Y., 2004. Crushing and plastic deformation of soils simulated using DEM. Géotechnique 54 (2), 131–141.
Cheng, H., Shuku, T., Thoeni, K., Yamamoto, H., 2017. Calibration of micromechanical parameters for DEM simulations by using the particle filter. In: EPJ Web of Conferences 140.
Clayton, C.R.I., 2011. Stiffness at small strain: research and practice. Géotechnique 61 (1), 5–37.
Cui, S.Q., Zhou, C., Liu, J.Q., Akinniyi, D.B., 2023. Stress effects on thermal conductivity of soils and heat transfer efficiency of energy piles in the saturated and unsaturated soils. Computers and Geotechnics 160, 105549.
Cundall, P., 1988. Computer simulations of dense sphere assemblies. Studies in Applied Mechanics. Elsevier 113–123.
da Cruz, F., Emam, S., Prochnow, M., Roux, J.N., Chevoir, F., 2005. Rheophysics of dense granular materials: discrete simulation of plane shear flows. Phys Rev E Stat Nonlin Soft Matter Phys 72 (2 Pt 1), 021309.
Dai, B.L., Zhou, C., Tang, A.M., Guayacán-Carrillo, L.M., 2024. A bounding surface model for anisotropic and structured soils under saturated and unsaturated conditions. Computers and Geotechnics 173, 106533.
Estrada, N., Taboada, A., Radjai, F., 2008. Shear strength and force transmission in granular media with rolling resistance. Physical Review E 78 (2), 021301.
Fu, P., Dafalias, Y.F., 2011. Study of anisotropic shear strength of granular materials using DEM simulation. International Journal for Numerical and Analytical Methods in Geomechanics 35 (10), 1098–1126.
Gong, J., Liu, J., 2017. Effect of aspect ratio on triaxial compression of multi-sphere ellipsoid assemblies simulated using a discrete element method. Particuology 32, 49–62.
Gong, J., et al., 2024. Effects of particle shape, physical properties and particle size distribution on the small-strain stiffness of granular materials: A DEM study. Computers and Geotechnics 165, 105903.
Gu, X., Yang, J., Huang, M., 2013. DEM simulations of the small strain stiffness of granular soils: effect of stress ratio. Granular Matter 15 (3), 287–298.
Gu, X., Zhang, J., Huang, X., 2020. DEM analysis of monotonic and cyclic behaviors of sand based on critical state soil mechanics framework. Computers and Geotechnics 128.
Guo, N., Zhao, J., 2013. The signature of shear-induced anisotropy in granular media. Computers and Geotechnics 47, 1–15.
Hartmann, P., Cheng, H., Thoeni, K., 2022. Performance study of iterative Bayesian filtering to develop an efficient calibration framework for DEM. Computers and Geotechnics 141.
Huang, X., Hanley, K.J., O'Sullivan, C., Kwok, C.Y., 2014. Exploring the influence of interparticle friction on critical state behaviour using DEM. International Journal for Numerical and Analytical Methods in Geomechanics 38 (12), 1276–1297.
Iwashita, K., Oda, M., 1998. Rolling Resistance at Contacts in Simulation of Shear Band Development by DEM. Journal of Engineering Mechanics 124 (3), 285–292.
Johnson, K.L., 1987. Contact mechanics. Cambridge University Press.
Kodicherla, S.P.K., et al., 2019. The influence of particle elongations on direct shear behaviour of granular materials using DEM. Granular Matter 21 (4), 86.
Le, N.B., Toyota, H., Takada, S., 2020. Evaluation of mechanical properties of mica-mixed sand considering inherent anisotropy. Soils and Foundations 60 (2), 533–550.
Li, X.S., Dafalias, Y.F., 2012. Anisotropic Critical State Theory: Role of Fabric. Journal of Engineering Mechanics 138 (3), 263–275.

Li, X.S., Dafalias, Y.F., 2015. Dissipation consistent fabric tensor definition from DEM to continuum for granular media. Journal of the Mechanics and Physics of Solids 78, 141–153.
Li, X., Yu, H.S., 2011. Tensorial characterisation of directional data in micromechanics. International Journal of Solids and Structures 48 (14–15), 2167–2176.
Li, Y., Otsubo, M., Kuwano, R., 2022. Interpretation of static and dynamic Young's moduli and Poisson's ratio of granular assemblies under shearing. Computers and Geotechnics 142.
Mindlin, R.D., Deresiewicz, H., 1953. Elastic spheres in contact under varying oblique forces.
Modenese, C., 2013. Numerical study of the mechanical properties of lunar soil by the discrete element method. Oxford University, UK.
Mohamed, A., Gutierrez, M., 2010. Comprehensive study of the effects of rolling resistance on the stress–strain and strain localization behavior of granular materials. Granular Matter 12 (5), 527–541.
Ng, C.W.W., Zheng, G., Ni, J., Zhou, C., 2020. Use of unsaturated small-strain soil stiffness to the design of wall deflection and ground movement adjacent to deep excavation. Computers and Geotechnics 119, 103375.
Nguyen, H.C., 2022. Discrete element method analysis of non-linear stiffness for granular media. Computers and Geotechnics 145.
Nie, J.Y. Cui, Y.F., Wang, G.D., Wang, R., Zhang, N.N., Zhang, L., Wu, Z.J., 2024. A comprehensive numerical investigation of multi-scale particle shape effects on small-strain stiffness of sands. Géotechnique, published online, doi: 10.1680/jgeot.23.00118.
Otsubo, M., O'Sullivan, C., 2018. Experimental and DEM assessment of the stress-dependency of surface roughness effects on shear modulus. Soils and Foundations 58 (3), 602–614.
Otsubo, M., O'Sullivan, C., Hanley, K.J., Sim, W.W., 2017. The influence of particle surface roughness on elastic stiffness and dynamic response. Géotechnique 67 (5), 452–459.
Ouadfel, H., Rothenburg, L., 2001. 'Stress–force–fabric' relationship for assemblies of ellipsoids. Mechanics of Materials 33 (4), 201–221.
Oztoprak, S., Bolton, M.D., 2013. Stiffness of sands through a laboratory test database. Géotechnique 63 (1), 54–70.
O'Sullivan, C., 2011. Particle-based discrete element modeling: geomechanics perspective. International Journal of Geomechanics 11 (6), 449–464.
Plassiard, J.-P., Belheine, N., Donzé, F.-V., 2009. A spherical discrete element model: calibration procedure and incremental response. Granular Matter 11 (5), 293–306.
Radjai, F., Roux, J.-N., Daouadji, A., 2017. Modeling Granular Materials: Century-Long Research across Scales. Journal of Engineering Mechanics 143 (4), 04017002.
Reddy, N.S., He, H., Senetakis, K., 2022. DEM analysis of small and small-to-medium strain shear modulus of sands. Computers and Geotechnics 141, 104518.
Rorato, R., Arroyo, M., Gens, A., Andò, E., Viggiani, G., 2021. Image-based calibration of rolling resistance in discrete element models of sand. Computers and Geotechnics 131.
Sandeep, C.S., Senetakis, K., 2018a. Effect of Young's Modulus and Surface Roughness on the Inter-Particle Friction of Granular Materials. Materials (Basel) 11 (2).
Sandeep, C.S., Senetakis, K., 2018b. Grain-scale mechanics of quartz sand under normal and tangential loading. Tribology International 117, 261–271.
Sandeep, C.S., He, H., Senetakis, K., 2018. An experimental micromechanical study of sand grain contacts behavior from different geological environments. Engineering Geology 246, 176–186.
Sitharam, T.G., Vinod, J.S., 2010. Evaluation of Shear Modulus and Damping Ratio of Granular Materials Using Discrete Element Approach. Geotechnical and Geological Engineering 28 (5), 591–601.
Sitharam, T.G., Vinod, J.S., Ravishankar, B.V., 2009. Post-liquefaction undrained monotonic behaviour of sands: experiments and DEM simulations. Géotechnique 59 (9), 739–749.
Šmilauer, V., et al., 2015. Yade Documentation, 2nd ed.
Sufian, A., Russell, A.R., Whittle, A.J., 2017. Anisotropy of contact networks in granular media and its influence on mobilised internal friction. Géotechnique 1–14.
Thornton, C., 2000. Numerical simulations of deviatoric shear deformation of granular media. Géotechnique 50 (1), 43–53.
Thornton, C., Antony, S.J., 1998. Quasi-Static Deformation of Particulate Media. Philosophical Transactions: Mathematical, Physical and Engineering Sciences 356 (1747), 2763–2782.
Thornton, C., Antony, S., 2000. Quasi-static shear deformation of a soft particle system. Powder technology 109 (1–3), 179–191.
Thornton, C., Zhang, L., 2006. A numerical examination of shear banding and simple shear non-coaxial flow rules. Philosophical Magazine 86 (21–22), 3425–3452.
Verdugo, R., Ishihara, K., 1996. The Steady State of Sandy Soils. Soils and Foundations 36 (2), 81–91.
Wang, R., Fu, P., Zhang, J.-M., Dafalias, Y.F., 2016. DEM study of fabric features governing undrained post-liquefaction shear deformation of sand. Acta Geotechnica 11, 1321–1337.
Wang, J.-P., Li, X., Yu, H.-S., 2017. Stress–Force–Fabric Relationship for Unsaturated Granular Materials in Pendular States. Journal of Engineering Mechanics 143 (9), 04017068.
Wensrich, C.M., Katterfeld, A., 2012. Rolling friction as a technique for modelling particle shape in DEM. Powder Technology 217, 409–417.
Wood, D.M., 1990. Soil behaviour and critical state soil mechanics. Cambridge University Press.
Wu, H., Gu, X., Hu, J., Zhou, Q., 2022. DEM simulation of small strain and large strain behaviors of granular soils with a coherent contact model. Granular Matter 24 (4), 125.
Yang, M., Taiebat, M., Mutabaruka, P., Radjai, F., 2021. Evolution of granular materials under isochoric cyclic simple shearing. Phys Rev E 103 (3–1), 032904.
Yimsiri, S., Soga, K., 2000. Micromechanics-based stress–strain behaviour of soils at small strains. Géotechnique 50 (5), 559–571.
Zhao, S., Zhou, X., 2017. Effects of particle asphericity on the macro-and micro-mechanical behaviors of granular assemblies. Granular Matter 19, 1–18.
Zhao, S., Evans, T.M., Zhou, X., 2018. Shear-induced anisotropy of granular materials with rolling resistance and particle shape effects. International Journal of Solids and Structures 150, 268–281.
Zhou, W., Xu, M., 2024. Microscopic analysis of the nonlinear stiffness of granular materials at small-to-medium strain. Computers and Geotechnics 165.
Zhou, C., Xu, J., Ng, C.W.W., 2015. Effects of temperature and suction on secant shear modulus of unsaturated soil. Géotechnique Letters 5 (3), 123–128.